

STRAIN RATE EFFECT ON TWIP/TRIP HIGH ENTROPY ALLOY

by

Omar-Mohammad-Marwan-El-Batal

A Thesis Presented to the Faculty of the  
American University of Sharjah  
College of Engineering  
In Partial Fulfillment  
of the Requirements  
for the Degree of  
  
Master of Science in  
Mechanical Engineering

Sharjah, United Arab Emirates

July 2021

## Declaration of Authorship

I declare that this thesis is my own work and, to the best of my knowledge and belief, it does not contain material published or written by a third party, except where permission has been obtained and appropriately cited through full and accurate referencing.

Signed.....Omar-Mohammad Marwan-El-Batal.....

Date..... Thursday, July 1, 2021.....

The Author controls copyright for this report.

The material should not be reused without the consent of the Author. Due acknowledgment should be made where appropriate.

© Year 2021

Omar-El-Batal

ALL RIGHTS RESERVE

## Approval Signatures

We, the undersigned, approve the Master's Thesis of Omar-Mohammad-Marwan-El-Batal

Title: strain rate effect on twip/trip high entropy alloy

Date of Defense: July,1,2021

<b>Name, Title and Affiliation</b>	<b>Signature</b>
------------------------------------	------------------

---

Dr. Wael Abuzaid

Assistant Professor, Department of Mechanical Engineering

Thesis Advisor

---

Dr. Maen Abdelqabder Alkhader

Associate Professor, Department of Mechanical Engineering

Thesis Co-Advisor

---

Dr. Farid Abed

Professor, Department of Civil Engineering

Thesis Committee Member

---

Dr. Mehmet Egilmez

Associate Professor, Department of Physics

Thesis Committee Member

---

Dr. Bassam Abu-Nabah

Associate Professor, Department of Mechanical Engineering

Thesis Committee Member

---

Dr. Mamoun Fahed Saleh Abdel-Hafez

Head

Department of Mechanical Engineering

---

Dr. Lotfi Romdhane

Associate Dean for Graduate Affairs and Research

College of Engineering

---

Dr. Sameer Al-Asheh

Interim Dean

College of Engineering

---

Dr. Mohamed El-Tarhuni

Vice Provost for Research and Graduate Studies

Office of Graduate Studies

## **Acknowledgment**

I want to thank my advisors Dr.WaelAbuzaid and Dr. MaenAlkhader, for providing the knowledge, support, guidance, and motivation throughout my studies and research stages. I am profoundly thank-full and beholden for their assistance, suggestions, and worthy discussions.

I would like to thank the professors of the Mechanical Engineering department who taught me the master-level courses with mighty teaching methods and skills. I appreciate their dignified advice and motivation.

I would like to thank Dr. Mehmet Egilmez from the physics department for teaching me how to use specific machines needed in my research.

I would like to thank the American University of Sharjah for providing the facilities for students to complete their research and also for providing the GRA/GTA which helped in completing the degree.

## **Dedication**

*I dedicate this thesis to my caring Father and in the memory of my loving Mother.*

## Abstract

High Entropy Alloys (HEA) present opportunities to develop new materials with outstanding mechanical properties. Through the careful selection of constituent elements along with optimized thermal processing for proper control of structure, grain size, and deformation mechanisms, many of the newly developed HEA systems exhibit superior strength and ductility levels across a wide range of temperatures, in particular at cryogenic deformation temperatures. Such a remarkable response has been attributed to the hardening capacity of HEA that is achieved through the activation of deformation twinning. More recent HEA compositions have considered phase transforming systems which have the potential for enhanced strengthening and therefore high strength and ductility levels. However, the strain rate sensitivity of such transforming HEA is not well understood and requires further investigation. In this study, the dynamic and quasi-static tensile properties of the non-equiatomic V10Cr10Fe45Co30Ni5 HEA were investigated temperatures ranging from 77K (196°C) to 573K (300°C). Depending on the deformation temperature, the considered HEA exhibits plasticity through either crystallographic slip, deformation twinning, or solid-state phase transformation. At 300°C, only slip mediated plasticity was observed for all the considered deformation rates. Deformation twinning was detected in samples deformed at room temperature (RT), while phase transformation, face-centered cubic to body-centered cubic, became more favorable at cryogenic deformation temperatures. At a deformation strain rate of  $1.32 \times 10^{-3}$  /s and 77K deformation temperature, the alloy reached an impressive tensile strength of around 1.2 GPa with a ductility exceeding 60%. Plastic deformation was accommodated in this case through phase transformation which consequently enabled superior strength and ductility. Both, the strain rate sensitivity (SRS) and strain hardening rates were shown to differ depending on the dominant deformation mechanism. For example, the SRS parameter  $m$  decreased as the deformation temperature dropped from RT ( $m = 0.05$ ) to 77K ( $m = 0.017$ ). Increasing the loading temperature to 300°C resulted in higher ductility, however at the expense of strength. Due to the absence of either twinning or transformation as hardening mechanisms, the HEA experienced a drop in strength reaching up to 23% at 300°C.

**Keywords:** *High entropy alloys; Strain rate sensitivity; TWIP; TRIP; Polycrystals; strain hardening.*

## Table of Contents

Abstract .....	6
Chapter 1. Introduction.....	12
1.1 Overview .....	12
1.2 Research motivation .....	16
1.3 Thesis Objective .....	17
Chapter 2. Literature Review and Background .....	19
2.1 HEA characteristics .....	19
2.1.1 Mechanical properties .....	19
2.1.2 Sluggish Diffusion. ....	19
2.1.3 Severe lattice distortion .....	20
2.2 Effect of temperature and strain rate .....	21
2.3 Flow stress models .....	24
2.3.1 Johnson-cook model.....	24
2.3.2 V-A flow stress model.....	25
2.4 Effects of TWIP and TRIP.....	26
Chapter 3. Methodology .....	29
3.1 Material preparation .....	29
3.2 Experimental tools.....	32
3.3 Experimental setup and procedure .....	33
Chapter 4. Results.....	35
4.1 Tensile properties in as-cast microstructure .....	35
4.2 Tensile properties – optimized microstructure .....	36
4.3 Crystal structure-observation of TRIP effect .....	39
4.4 Strain rate sensitivity and hardening response .....	41
4.5 Fracture surface analysis .....	45
4.6 Modelling .....	46
4.6.1 J-C model. ....	46
4.6.2 V-A model .....	54
Chapter5. Conclusion .....	61
Reference.....	62
Vita .....	67

## List of Figures

Figure 1.1: Ashby plot of fracture toughness vs. yield strength plot of the mostcommonly used structural materials. HEAs (top right) show an outstanding combination of damage-tolerant mechanical properties compared with other materials [9].....	14
Figure 1.2: Typical stress-strain curves of cantor-alloy at room and cryogenic temperatures.[10].....	14
Figure 1.3: Single crystalline VFeCoCrNi HEA deformed in tension. The EBSD grain map shows the TWIP effect with clear development of deformation twinning. The full-field strain contour plot (right) show the localizations associated with TRIP following deformation and cryogenic[12] .....	16
Figure 1.4: HEA popularity over the years .....	17
Figure 2.1: Deep traps in HEAs /source: adapted from [1] .....	19
Figure 2.2 Schematic of lattice distortion due to addition of multiple elements with different atomic size[5] .....	20
Figure 3.1: (a) SEM backscatter image showing the grain structure of cast material. (b) the corresponding grain orientation map .....	29
Figure 3.2: Dog-bone-schematic .....	30
Figure 3.3: encapsulated sample .....	30
Figure 3.4: (a) XRD Data showing FCC peaks, (b), EDX data confirming the non-equiatomic composition of the HEA, (c) EDX mapping confirming the homogenous distribution in the material. ....	31
Figure 3.5: Dog bone with speckle pattern (magnified) .....	32
Figure 3.6: Experimental setup .....	33
Figure 3.7: Dog bone grips .....	34
Figure 3.8: aluminum box for experiments in LN .....	34
Figure 4.1: Preliminary Stress-Strain curves .....	36
Figure 4.2: Engineering stress-strain curves .....	38
Figure 4.3: XRD of rolled and solution treated specimen .....	39
Figure 4.4: XRD of deformed samples at different testing conditions .....	40
Figure 4.5: True stress-strain curves (left), Strain Hardening (right)-RT .....	44
Figure 4.6: True stress-strain curves (left), Strain Hardening (right)-LN.....	44
Figure 4.7: True stress-strain curves (left), Strain Hardening (right)-300°C.....	44
Figure 4.8: Fracture surfaces of tensile specimens at RT a) 1.32e-3/s, b)0.66/s, c)1.32/s .....	45
Figure 4.9: Fracture surfaces of tensile specimens at LN a) 1.32e-3/s, b)0.66/s, c)1.32/s .....	46
Figure 4.10: Fracture surfaces of tensile specimens at 300°C a) 1.32e-3/s, b)1.32/s ..	46
Figure 4.11: n and B curve fitting .....	48
Figure 4.12: C curve fitting .....	49
Figure 4.13: m curve fitting .....	50
Figure 4.14: JC flow stress model at RT a)1.32e-/s, b) 0.66/s and c) 1.32/s .....	52
Figure 4.15: JC flow stress model at LN a)1.32e-/s, b) 0.66/s and c) 1.32/s.....	53
Figure 4.16: flow stress model at 300°C a)1.32e-/s, b) 1.32/s.....	54

Figure 4.17:log-log curve of the True stress and True strain.....	55
Figure 4.18: $\mu_0$ linear fit. ....	56
Figure 4.19:VA flow stress model at RT a)1.32e-/s, b) 0.66/s and c) 1.32/s.....	58
Figure 4.20:VA flow stress model at LN a)1.32e-/s, b) 0.66/s and c) 1.32/s .....	59
Figure 4.21:VA flow stress model at 300°C a)1.32e-/s, b) 1.32/s.....	60

## List of Tables

Table 1:lattice parameter at XRD peaks. ....	31
Table 2:Testing Strain rates and temperatures.....	35
Table 3: $V_{10}Fe_{45}Co_{30}Cr_{10}Ni_5$ mechanical properties.....	38
Table 4: $V_{10}Fe_{45}Co_{30}Cr_{10}Ni_5$ mechanical properties.....	39
Table 5:Variation of strain rate sensitivity m with temperature. ....	41
Table 6:J-C model parameters .....	51
Table 7:V-A calculated model parameters .....	56
Table 8: remaining parameters obtained from literature[37] for FCC alloy.....	57

## **List of Abbreviations**

BCC	Body-Centered Cube
DP	Dual Phase
FCC	Face-Centered Cube
HEA	High Entropy Alloy
LN	Liquid Nitrogen
MPEA	Multi Principal Element Alloy
RT	Room Temperature
SF	Stacking Fault
SFE	Stacking Fault Energy
TRIP	Transformation Induced Plasticity
TWIP	Twinning Induced Plasticity

## Chapter 1. Introduction

### 1.1 Overview

Enhancing material properties through alloying has been practiced for hundreds of years. For example, adding a few percent of copper by weight to silver, which is very soft in its pure state, produced sterling silver which has improved mechanical properties[1]. The need to develop new materials with enhanced properties has fueled major research activities to overcome existing limitations. Metals and metallic alloys are of particular importance due to their desirable properties and wide use in practical applications. Although engineering alloy properties through composition control and heat treatment is not new and go back hundreds of years, significant developments and advancements were made in the last century by utilizing new experimental and analytical tools. A large number of new alloy systems were developed for advanced applications through proper control and understanding of microstructure and deformation mechanisms. For example, Ni-based super-alloys that are optimized for high-temperature applications[2], Maraging steels which exhibit high strength and toughness levels[3], twinning induced, and Transformation induced plasticity steels (TWIP and TRIP) where high strength and ductility levels are attained through the additional hardening introduced through the activation of these two important deformation mechanisms[4]. Generally speaking, the use of a single principal element, present at large a percentage, in addition to alloying elements at lower percentages, has been the common alloy design methodology in the aforementioned systems and in virtually all structural alloys. Despite the notable advances made utilizing this alloying principle, recent efforts have ventured outside these well-established guidelines in an attempt to achieve new alloy systems with superior properties.

The recent development of high entropy alloys (HEAs) and medium entropy alloys (MEAs), also known as multi-principle element alloys (MPEAs), has challenged the well-known alloy design principle, which relies on the use of predominantly a single alloying element[5]. Through the use of multiple principal elements, new systems have been introduced that exhibits remarkable properties. This group of alloys was first introduced in 2004 by professor Jien-Wei Yeh, and they are defined as alloys containing five or more principal elements, each having 5% to 35 % in an equiatomic near-

equiatomic, or non-equiatomic compositions[6]. In the case of HEA, the resulting mixing entropy is higher than  $1.6R$  ( $R$  is the gas constant), where MEA has magnitudes between  $R$  and  $1.6R$  [1][7]. In general, the high entropy in these alloys promotes the formation of a solid solution phase and reduces the Gibbs free energy  $G=H-TS$  ( $T$  is the temperature,  $S$  is the entropy, and  $H$  is the enthalpy) at high temperatures. Consequently, the number of phases generated is smaller, which will improve the compatibility between elements and results in the formation of simple and stable single-phase structures. In addition, the high entropy will decrease the electro negativity difference and thus help avoid phase separation [1][3][4]. A wide range of compositions and resulting crystal structures have been reported, including FCC (Face-Centred-Cubic), BCC (Body-Centred-Cubic), HCP (Hexagonal Close Packed ), or a mixture of them [1]. The earlier compositions, sometimes referred to as first-generation HEAs, were focused on single-phase structures. However, more recent works have also considered compositions with dual or multi-phase microstructures, also known as the second generation of HEAs, while seeking optimized and further enhancements of properties.

The use of a relatively large number of principle elements in MPEAs results in some unique characteristics in these alloy systems. Some of the characteristics include the high-entropy effect, sluggish diffusion effect, severe lattice distortion, and the cocktail effect, in which properties are undoubtedly related to the properties of the constituent elements. For example, adding Nb (refractory elements) will enhance the mechanical properties at high-temperatures. However, it should be emphasized that the interaction between the various alloying elements may result in exceptional properties that defy well-known trends as shown for many of the investigated MPEA compositions [8].

From a “mechanical properties” perspective, various HEAs show exceptional fatigue and fracture resistance with high strength and ductility at cryogenic temperatures (see **Fig. 1.1**). Such a unique combination of desirable properties positions MPEAs as perfect candidates for cryogenic applications. For example, the well-known and heavily investigated equiatomic CoCrFeMnNi (also referred to as the Cantor alloy) exhibits exceptional strength, ductility, and toughness levels, all at the same time. At low temperatures (e.g., 77 K or liquid nitrogen temperature), the alloy shows a

remarkable enhancement in strength along with an unconventional improvement in ductility (see **Fig. 1.2**). Such desirable properties have been linked to the high strain hardening capacity in this system, enabled by mechanical twinning, which delays the onset of necking and allows for excellent ductility [1].

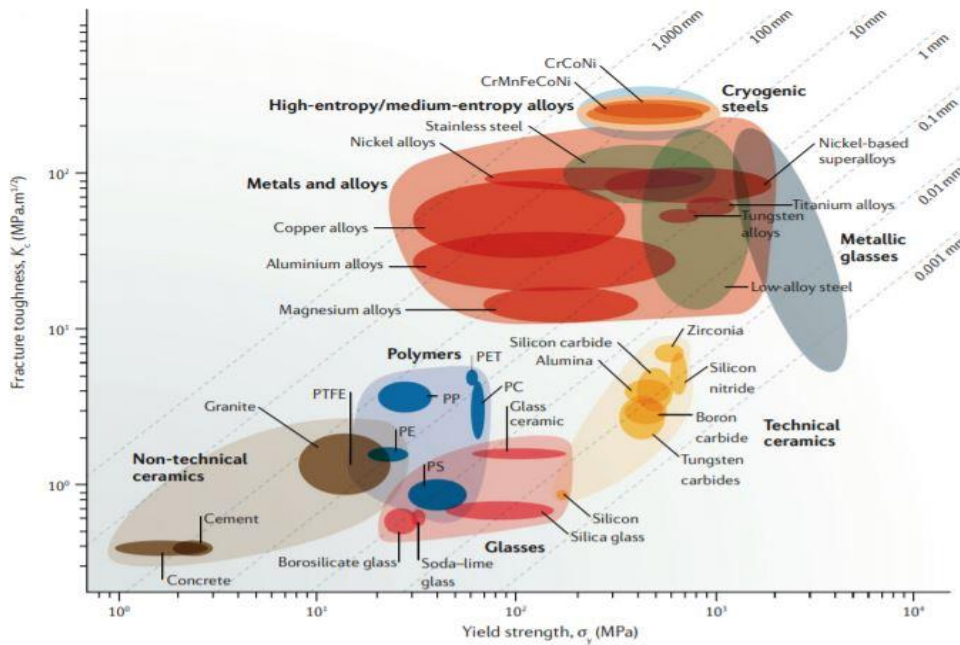


Figure 1.1: Ashby plot of fracture toughness vs. yield strength plot of the most commonly used structural materials. HEAs (top right) show an outstanding combination of damage-tolerant mechanical properties compared with other materials [9]

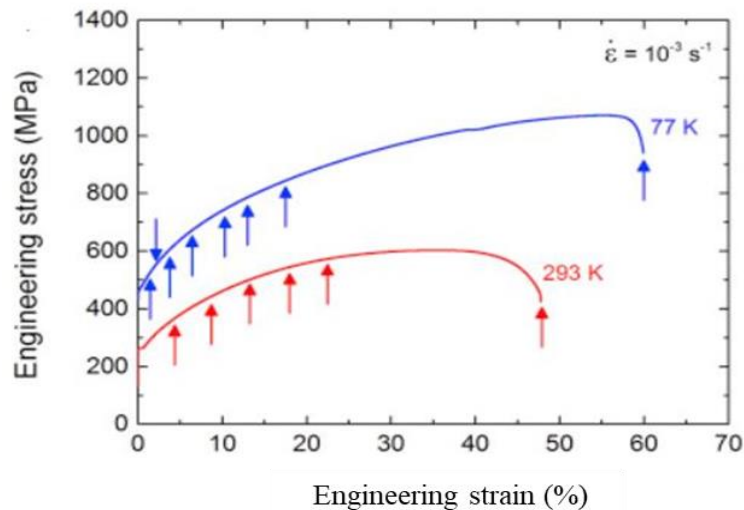


Figure 1.2: Typical stress-strain curves of cantor-alloy at room and cryogenic temperatures. [10]

The Cantor alloy has a single-phase FCC microstructure. Single-phase compositions with BCC structures have also been considered in the literature. In general, the addition of Al to Cantor alloy-based systems (e.g., AlCoCrFeNi HEA) stabilizes the BCC structure at the expense of the FCC phase. The ductility of such systems with BCC crystal structures is generally inferior compared to their FCC counterpart. Some of the refractory HEAs also have BCC crystal structures; for example, Nb<sub>25</sub>Mo<sub>25</sub>Ta<sub>25</sub>W<sub>25</sub> and V<sub>20</sub>Nb<sub>20</sub>Mo<sub>20</sub>Ta<sub>20</sub>W<sub>20</sub>. These alloys, although inferior in terms of ductility compared to the FCC-based structures, offer better resistance to high temperatures softening and exhibit enhanced thermal stability [1]. Resolving the issue of inferior ductility in BCC-based HEA requires further research.

Revealing the fundamental reasons for the remarkable mechanical properties of HEAs has been the subject of many studies. The role of deformation twinning (TWIP effect) has been emphasized as this deformation mechanism enables additional hardening, increases strength levels, and eventually results in enhanced ductility. Stacking fault energy (SFE), which is defined as the energy carried by the interruption of normal stacking sequence [11], plays a major role in influencing the deformation mechanism; namely, Twinning Induces Plasticity and Transformation Induced Plasticity. Many HEAs show TWIP at cryogenic temperatures, which explains the enhanced ductility.

Some of the newly developed HEAs exhibit a combined TWIP and TRIP effects, depending on the deformation temperature. The FCC – HCP transforming compositions comprise the majority of MPEs exhibiting TRIP (e.g., Fe<sub>40</sub>Mn<sub>40</sub>Co<sub>10</sub>Cr<sub>10</sub>, Cr<sub>20</sub>Mn<sub>24</sub>Fe<sub>30</sub>Co<sub>20</sub>Ni<sub>6</sub>, and Cr<sub>20</sub>Mn<sub>15</sub>Fe<sub>34</sub>Co<sub>20</sub>Ni<sub>11</sub>) [12][13][14]. In addition to the FCC-HCP TRIP alloys, unique and interesting FCC-BCC TRIP HEAs have recently been reported for a limited number of compositions. For instance, the non-equiatomic Fe<sub>45</sub>Co<sub>30</sub>Cr<sub>10</sub>V<sub>10</sub>Ni<sub>5</sub>-xMnx (x = 0, 2.5, and 5 at. %) HEA and more recently V<sub>10</sub>Fe<sub>45</sub>Co<sub>30</sub>Cr<sub>10</sub>Ni<sub>5</sub>, both exhibited FCC-BCC TRIP effect at cryogenic temperatures [15][16][17]. Understanding the hardening effects introduced by introducing the BCC phase and its temperature and deformation rate effects is important to optimize the mechanical properties of these alloys and assist in the efforts aimed to resolve the ductility issues in BCC-based HEA in general. This work aims to address this issue by investigating a novel TWIP/TRIP HEA (FCC – BCC). In

particular, VFeCoCrNi HEA (see **Fig. 1.3**) was thoroughly investigated to shed insight into the strength, hardening, and ductility effects of the stress-induced phase transformation and its temperature and deformation rate dependencies.

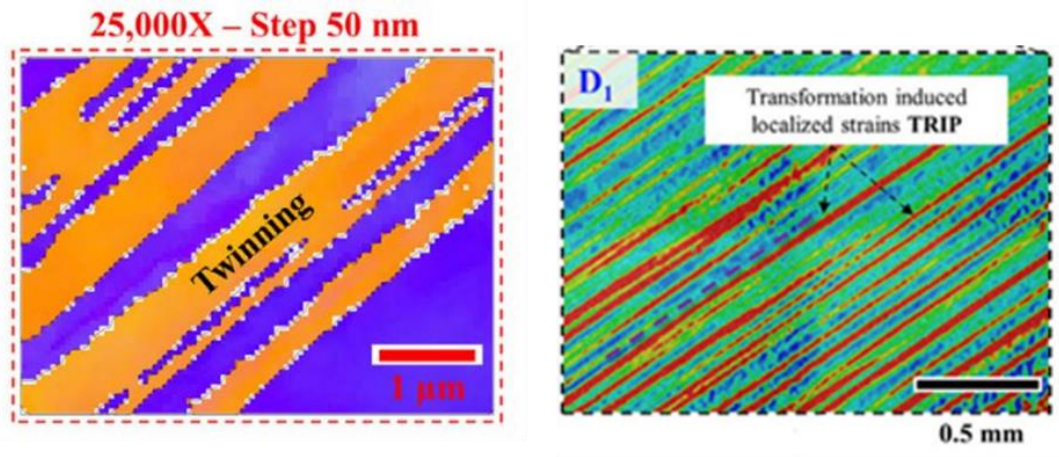


Figure 1.3: Single crystalline VFeCoCrNi HEA deformed in tension. The EBSD grain map shows the TWIP effect with clear development of deformation twinning. The full-field strain contour plot (right) shows the localizations associated with TRIP following deformation and 77K [4]

## 1.2 Research motivation

The new design principles offered by HEAs (i.e., using multiple principal elements with high content) allow for a large number of systems to be developed and optimized to exhibit unique and desirable properties. This extends beyond just mechanical to almost all relevant properties for an extremely wide range of applications (e.g., thermal, corrosion, oxidation, magnetic, etc.). As a result, HEAs have gained remarkable popularity ever since their discovery in 2004 by Jien-Wei Yeh. **Fig 1.4** shows the number of published papers focused on HEAs over the past decade. The published works highlight the significant and increasing interest in this class of materials. In terms of mechanical properties, which this study is focused on, HEAs exhibiting TWIP have been heavily investigated in the literature. Compositions with the additional strengthening due to phase transformation (i.e., TRIP MPEA) are limited and not fully explored. The majority of the considered TRIP HEAs exhibit an FCC to HCP phase transformation (e.g., FeMnCoCr[13]). This work, however, is focused on a novel MPE, V10Cr10Fe45Co30Ni5. Which exhibits a combined TWIP at room temperature and FCC to BCC TRIP effect at cryogenic temperatures. The nature of

Transformation has been revealed recently in the literature. However, the temperature and deformation rate effects on the tendency of the alloy to exhibit slip, twinning, or phase transformation have not been fully explored. This study attempts to elucidate the effect of deformation temperature and strain rate on the mechanical properties, both experimentally and analytically.

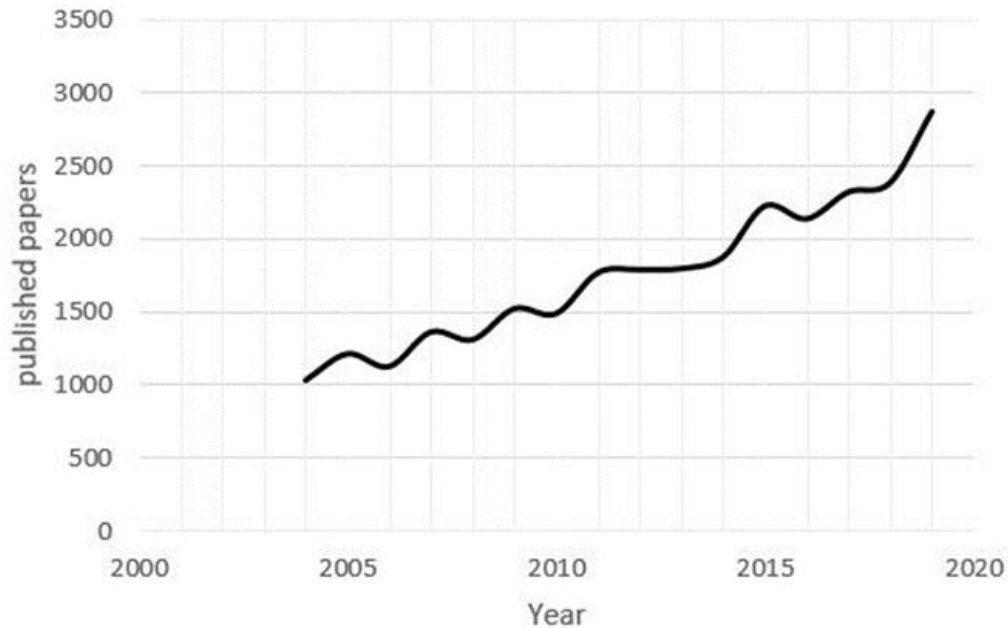


Figure 1.4:HEA popularity over the years

### 1.3 Thesis Objective

This work aims to investigate the deformation behavior of non-equiatomic high entropy alloy (HEA),  $V_{10}Fe_{45}Co_{30}Cr_{10}Ni_5$ , at temperatures ranging between 77K and 293K and various loading rates. Depending on deformation temperature, the alloy may exhibit either TWIP or TRIP effects. The strain rate sensitivity is expected to differ depending on the dominant deformation mechanism (i.e., twinning or Transformation induced plasticity). This aspect will directly impact the hardening levels, hardening capacity, and ductility levels of this system. Therefore, developing a comprehensive understanding of strain rate sensitivity is crucial from a practical perspective. The work will utilize polycrystalline specimens and aims to accomplish the following objectives:

- Optimize the mechanical properties of as-cast  $V_{10}Fe_{45}Co_{30}Cr_{10}Ni_5$  HEA through rolling and heat treatment.

- Study the mechanical properties, tension, at different deformation temperatures and strain rates.
- Study the hardening rates and the effect of the dominant deformation mechanism on the resulting strength and ductility.
- Evaluate the crystal structure using x-ray diffraction to study and quantify the development of the BCC phase due to TRIP.
- Evaluate the Strain Hardening curves to develop an understanding of how TWIP alloys behave.
- Calibrate various relevant constitutive models to capture the temperature and strain rate sensitivity in this system

## Chapter 2. Literature Review and Background

### 2.1 HEA characteristics

**2.1.1 Mechanical properties.** HEAs are great candidates for structural applications due to their excellent resistance to softening at high temperatures, exceptional ductility, high wear resistance, superior damage tolerance, and high fracture toughness at cryogenic temperatures. The favorable properties at cryogenic temperatures (i.e., high strength, ductility, and toughness) have been attributed to the alloy's high strain hardening capacity, induced by the transition from dislocation mediated plasticity to deformation-induced Nano-twinning (i.e., TWIP effect). Also, at room temperature, Nano-twinning was observed under high-pressure torsion and high strain levels. Nano-twinning plays a remarkable role and is expected to increase the strain hardening by the introduction of new interfaces in the material that would hinder dislocation slip [18]. The higher strength levels enabled by twinning delay the onset of necking and results in higher ductility levels.

**2.1.2 Sluggish Diffusion.** Recent studies showed that the self-diffusion coefficient of elements is much lower in HEAs compared to other traditional alloys. Professor Jien-Wei Yeh designed a diffusion couple that enabled him to show that FeMnCoCrNi had the smallest diffusion coefficient, indicating that HEAs have a lower diffusion rate than conventional alloys due to the lattice distortion and the interaction between atoms [1].

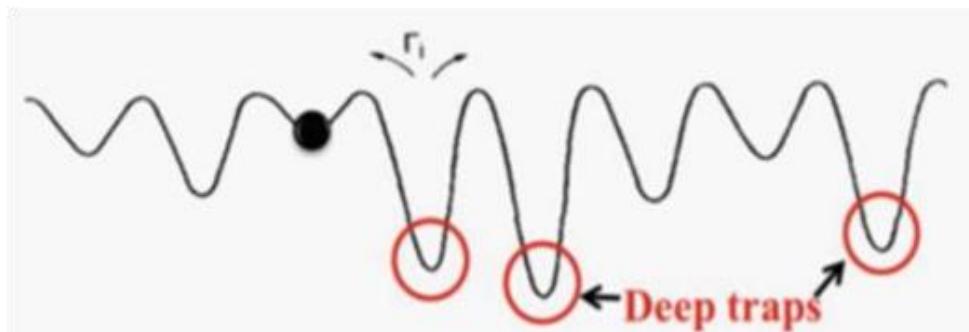


Figure 2.1: Deep traps in HEAs /source: adapted from [1]

In addition, the formation of new phases is affected by the sluggish diffusion effect. HEAs mainly diffuse through vacancy mechanisms due to different atoms

having different melting points and different bond strengths. Hence atoms with strong mobility are the most likely to diffuse into vacancy. The diffusion of atoms is a process of continuous vacancy filling. If the energy is reduced after filling the vacancy, then the atoms will have to use more energy to continue diffusion. If the energy is increased, it becomes difficult for the diffusing atom to fill in a vacancy site. Consequently, the HEA diffusion rates and phase transformation rates are reduced. In some HEAs, there are deep traps that aid in the slow atom diffusion, these traps can be seen in **Fig 2.1**

**2.1.3 Severe lattice distortion.** High Entropy Alloys are made of multiple elements; each element has a different atomic size. These differences in atomic sizes will lead to the distortion of the lattice resulting in relatively large lattice strains (see Fig 2.2). This large lattice distortion affects the HEAs properties. For example, lattice distortion delays dislocation motion leading to a significant solid solution strengthening effect. However, if the size of the atoms is excessively large, the distortion will be too high, which can result in lattice collapse (formation of amorphous phase).

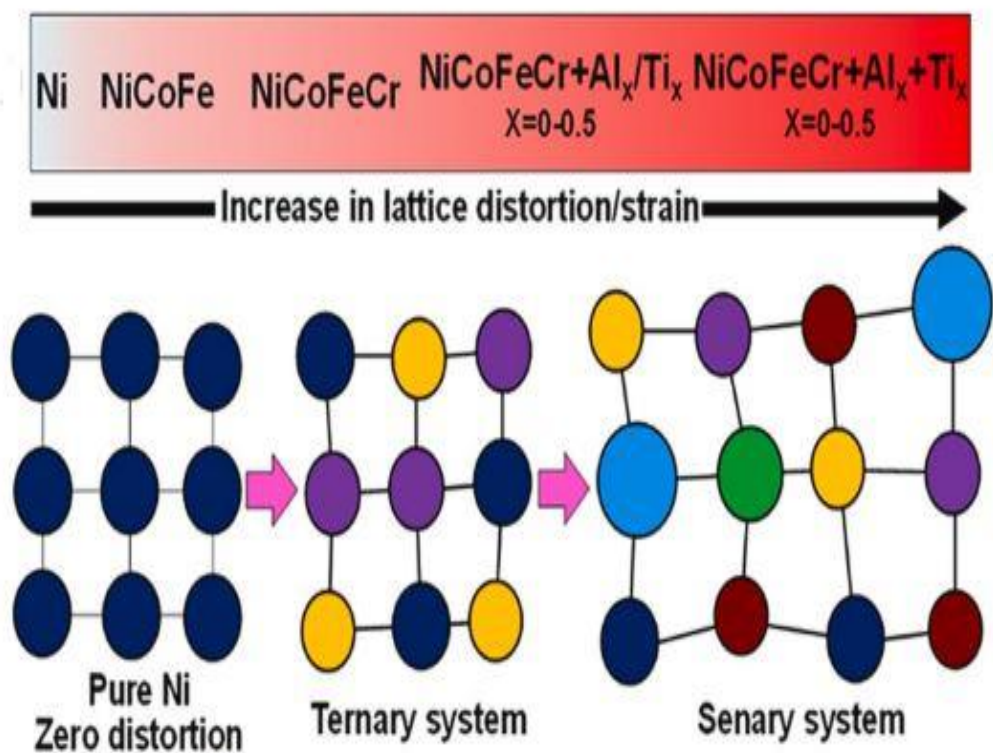


Figure 2.2 Schematic of lattice distortion due to addition of multiple elements with different atomic size[5]

## 2.2 Effect of temperature and strain rate

Multiple factors affect the mechanical properties of HEAs. However, deformation temperature, deformation strain rate, and grain size are the most critical. Temperatures ranging from cryogenic (77K) to high temperatures (773K) and deformation rates from slow to ultra-high strain rates can have been shown to significantly alter the properties of the HEA like strength and ductility. For example, the fine-grained (2.8 $\mu\text{m}$  grain size) Fe<sub>50</sub>Mn<sub>30</sub>Co<sub>10</sub>Cr<sub>10</sub> [19] dual-phase-HEA exhibited yield strength of (300 MPa) and ultimate tensile strength of (800 MPa) compared with its counterpart coarse-grained alloy that only exhibited a yield strength of (150 MPa) and ultimate tensile strength of (600 MPa). Both alloys have shown a 60% increase in elongation when subjected to different strain rates of  $5 \times 10^{-3}/\text{s}$ ,  $1 \times 10^{-3}/\text{s}$ ,  $5 \times 10^{-4}/\text{s}$ , and  $1 \times 10^{-4}/\text{s}$ . Basu et al. studied two-grain sizes of this alloy and found that along with the increase in elongation, the yield strength of the coarse-grained sample was 50% less than that of the fine-grained sample. To confirm these results, Basu subjected both samples to strain jump and found that the material was not sensitive to the strain rate and behaved in the same way. Z.F.He et al. found that as the strain rate increased from 0.001/s to 1000/s, the Fe<sub>50</sub>Mn<sub>30</sub>Co<sub>10</sub>Cr<sub>10</sub> HEA uniform elongation, yield strength, and ultimate tensile strength significantly improved [11]. Z.F.He et al. also studied how the temperature at cryogenic and room conditions with constant strain rate affects the Fe<sub>40</sub>Mn<sub>40</sub>Co<sub>10</sub>Cr<sub>10</sub>. It was found that the alloy's ductility and strength increased as the temperature decreased from room to cryogenic. This observation was attributed to the reduction in stacking fault energy at lower temperatures which is conducive to mechanical twinning [8]. Z. Wang et al. found that at cryogenic temperature, the Fe<sub>49.5</sub>Mn<sub>30</sub>Co<sub>10</sub>Cr<sub>10</sub>C<sub>0.5</sub> HEA showed a very high strain hardening which increased the strength, UTS, and consequently resulted in 50% increase in elongation [20].

The equiatomic FeMnCoCrNi Cantor alloy, which is the first, reported HEA and is up to date the most heavily, investigated composition, exhibits pronounced strength-temperature dependence. For example, decreasing the deformation temperature from room temperature to a cryogenic temperature of 77K results in doubling the strength [21]. However, the material strength has lower strain rate dependence. It should be noted that this composition deforms by slip, primarily at room temperature or above, and twinning at cryogenic temperatures. T. Zhang et al.

developed a non-equiatomic HEA Fe<sub>67</sub>Co<sub>8.25</sub>Cr<sub>8.25</sub>Ni<sub>8.25</sub>Mn<sub>8.25</sub> wt.% composition which exhibits a TRIP effect. The material was tested at a constant strain rate of 0.0001/s. A significant increase in the UTS during FCC to BCC transformation was observed compared to the initial FCC phase[22]. W. Huo et al. concluded that by increasing the strain rate, the UTS, fracture strain, strength, ductility, and hardness tend to increase for the CoCrFeNi HEA [18]. Another publication by S. Gangireddy et al. Studied the microstructural dependence of strain rate sensitivity for Al<sub>0.1</sub>CoCrFeNi HEA. The study concluded that samples tested at a low strain rate exhibited a low yield strength and that the strain rate sensitivity was highly dependent on the microstructure of this FCC HEA[23]. Ultra-high strain rates were also used to test the strain rate sensitivity of various HEAs (tensile and compression). S. Zhang et al. conducted a compression loading using a split Hopkinson pressure bar on TiZrHfNbTaMox (x= 0.25, 0.5 and 0.75) refractory high entropy alloy (RHEA) with strain rates from 2100 to 6000/s. It was observed that the alloy showed an increase in yield strength and good plasticity as the strain rate increased as well as ultra-high strain hardening effect[24]. Similarly, R. Sonkusare et al. used the same method to study CoCuFeMnNi HEA. This composition exhibited high strain hardening levels induced by deformation twinning at high deformation rates. [25].

The co-existence of ductile and brittle fracture mechanisms was found in the TaNbHfZrTi RHEA under an ultra-high strain rate of 2600/s as well as at cryogenic temperature (77K). Higher temperatures also promoted the strain hardening of the alloy along with excellent dynamic compression properties[26]. BCC (VNbMoTaW and NbMoTaW) HEAs showed lower SRS (strain rate sensitivity) in compression compared to FCC (FeCoNiCuPd and CrMnFeCoN) HEA, over the same range of strain rates 0.001/s, 0.0001/s and 0.01/s[27]. Y.H jo et al. examined V<sub>10</sub>Cr<sub>10</sub>Fe<sub>45</sub>Co<sub>30</sub>Ni<sub>5</sub> HEA at 0.001/s and 1000/s and concluded that the stress for twinning is less sensitive to strain rate and temperature compared to slip. BCC martensite decreased with the increase of strain rate at cryogenic temperatures. [16].

I.V. Kireeva et al. studied the tensile behavior of CoCrFeMnNi HEA at cryogenic temperature (77K). It was concluded that deformation twinning determines the strain hardening of the HEA at 77K. The development of twinning took place predominantly at 77K, resulting in high strain hardening and, consequently, a ductile

fracture [28]. Similar observations were also reported by W. Fu et al. for CrMnFeCoNi[29].

The Fe<sub>40</sub>Mn<sub>40</sub>Co<sub>10</sub>Cr<sub>10</sub> Single crystal (SC) HEA was investigated along the [111], [001], and [123] orientations to reveal the deformation mechanisms responsible for the different hardening stages. The alloy exhibited strong orientation dependence under room temperature deformation due to the activation and complex interaction between twinning and planar slip. However, the alloy in the [111] orientation exhibited exceptional strain hardening coefficient due to the interaction of multiple slip systems, alongside significant ductility due to the formation of Nano-twins. Plastic deformation was observed in the [123] orientation caused by both slip and Nano-twins coexistence. This was absent in [001] orientation [30]. Al<sub>0.3</sub>CoCrFeNi and CoCrFeNi single crystals were grown and tested at strain rates of 1.7 x 10<sup>-4</sup> /s, 1.7 x 10<sup>-5</sup> /s, 1.7 x 10<sup>-4</sup> /s, 1.7 x 10<sup>-3</sup> /s, and 1.7x10<sup>-4</sup> /s by Yasuda et al. It was found that flow stress of the single crystal alloy that contains aluminum decreased as the deformation temperature increased from 93K to 1273K. Comparing this alloy with its counterpart (CoCrFeNi) led to the discovery that the flow stress is much lower at 873K than the flow stress of (Al<sub>0.3</sub>CoCrFeNi) at that same temperature [31].

I.V. Kireeva et al. studied the same alloy in [32][33] as Yasuda (Al<sub>0.3</sub>CoCrFeNi). Tensile specimens were investigated over a range of temperature (77 to 973K) to report the mechanical behavior of the alloy along with the effect of  $\gamma'$  - phase particles and orientation dependence. The research revealed that the  $\gamma'$  -phase particles lead to the development of a planar structure. A reduction in the value of strain hardening coefficient and the localization of deformation was observed in one slip systems due to the increase in plasticity. The alloy also showed a planar dislocation with dislocation pile-ups under tensile strain in a range of temperatures of (77K-423K). In the range of (203K-573K), the strain hardening coefficient depends on the orientation and temperature. At the orientation of [001] with a temperature range of (203K-573K) and at the orientation of  $[\bar{1}11]$  with a temperature range of (423K and 573K), the strain hardening coefficient in the linear stage did not depend on temperature. At lower temperatures of (203K-296K), the  $[\bar{1}11]$  exhibits an increase in the strain rate hardening coefficient. Kireeva also concluded that in the  $[\bar{1}11]$  orientation, deformation twinning was found along with the [011] orientation at 77K. The activation of twinning

increased the strain hardening coefficient. Ma et al. also investigated the single crystal (Al<sub>0.3</sub>CoCrFeNi) HEA and reported 80% elongation with a prominent work-hardening exponent and remarkable homogenous plasticity. The single-crystal alloy at [001] orientation revealed a lower elastic module than its as-cast counterpart (multiple orientations), along with less plastic strain incompatibility [34].

I.V. Kireeva et al. also investigated the effect of twinning on the orientation dependence of equiatomic CoCrFeMnNi single-crystal HEA, at 77K under a constant strain rate of 4x10<sup>-4</sup>/s. Kireeva concluded that the alloy at 77K achieved high strain hardening during twinning and suppression of slip and stress relaxation. The  $[\bar{1}11]$ ,  $[\bar{1}23]$  and [011] crystal orientation demonstrated ductile fracture at 77K due to the decrease in the strain hardening during the simultaneous formation of twins[35]. Kireeva also showed that in the CoCrFeMnNi single-crystal HEA ,stacking faults and twinning in [001] orientation were detected along with an increase in the strain hardening coefficient under cryogenic temperature (77K)[7].

## 2.3 Flow stress models

**2.3.1 Johnson-cook model.** In recent years, the Johnson-cook model has been widely used to calculate flow stress due to its advantage of simple form, small calculation quantity, and fast calculation speed. Johnson-cook model has Five parameters; each parameter represents an independent material property, these parameters are A, B, C, n, and m. This model was first introduced by Johnson and cook in 1983 to describe the relationship between stress and strain in metals under high strain rates, large deformations and high temperatures[36]. The Johnson-cook model can be seen in Eq1

$$\sigma = (A + B\varepsilon^n)(1 + C \ln\dot{\varepsilon}^*)(1 - T^{*m}) \quad (1)$$

Johnson-Cook stress model

where

$$T^* = \frac{T - T_r}{T_m - T_r} \quad (2)$$

$$= \frac{\dot{\varepsilon}}{\dot{\varepsilon}_r} \quad (3)$$

$\sigma$  equivalent true stress,  $\varepsilon$  equivalent true strain,  $\dot{\varepsilon}$  strain rate,  $\dot{\varepsilon}_r$  Reference strain rate,  $T_m$  melting point,  $T_r$  reference temperature,  $A$  is the yield stress under reference

deformation.  $\mathbf{B}$  is the strain hardening constant,  $\mathbf{n}$  is the strain hardening exponent,  $\mathbf{C}$  is the strain rate strengthening coefficient, and  $\mathbf{m}$  is the thermal softening coefficient.

**2.3.2 V-A flow stress model.** V-A model is another flow stress model developed by Voyiadjis and Abed [37], to simulate the flow stress in pure FCC and BCC metals based on their microstructure at high and low strain rates and temperatures. V-A model also contains material parameters; these parameters are related and physically defined to nano- and micro-structure quantities. This model accommodates the dependence of temperature and strain rate on the deformation by relating every coefficient in the constitutive Equation to the microstructure.

$$\sigma = Y_a + (\tilde{\mathbf{B}}\varepsilon^n_p)[1 - (\beta_1(\varepsilon_p)\mathbf{T} - \beta_2\mathbf{T}\ln \frac{\dot{\varepsilon}_p}{\varepsilon_p \sigma^q})^{1/p}] \quad (4)$$

V-A flow stress model

$$\tilde{\mathbf{B}} = m\alpha_o \mu_o \frac{b^2}{A''_o} \quad (5)$$

hardening parameter

where  $\mathbf{Y}_a$  is the athermal stress,  $\tilde{\mathbf{B}}$  is the hardening parameter,  $\alpha_o$  is a constant which represents the portion of the shear modulus  $\mu_o$ ,  $m$  is the orientation factor that relates the shear stress to the normal stress,  $\mathbf{b}$  is the magnitude of the Burgers vector,  $\varepsilon_p$  is the strain,  $\mathbf{A}_o$  is the activation area,  $\dot{\varepsilon}$  is strain rate,  $\mathbf{T}$  is the temperature in  $\mathbf{K}$ ,  $\beta_1$ , and  $\beta_2$  are defined as follows.

$$\beta_1 = \frac{k}{G_o} \ln(1 + C_1(1 - \exp(-k_a \varepsilon_p))) \quad (6)$$

Mobile dislocation density

$$\beta_2 = \frac{k}{G_o} \quad (7)$$

constant

where  $\mathbf{k}$  is Boltzmann constant,  $\mathbf{G}_o$  is the Gibbs energy, and  $\mathbf{C}_1$  defined as

$$C1 = f \frac{M}{k_a \rho_{mi}} \quad (8)$$

where  $M = 1/b$  is the factor,  $l$  is the dislocation mean free path, the fraction  $f$ , which represents the mobile portion amount of the total dislocation density, is assumed constant for simplicity of the determination of the parameters,  $\rho_m$  is the dislocation density.  $k_a$  is the dislocation annihilation factor which may depend on both the temperature and strain rate.

#### 2.4 Effects of TWIP and TRIP

Plastic deformation through dislocation slip is the primary deformation mechanism in most engineering alloys. Hardening is typically achieved through dislocation multiplication and dislocation interactions with grain boundaries and other dislocations. Deformation twinning (TWIP) and phase induced phase transformation (TRIP) are other mechanisms to accommodate plastic deformation. Not all alloys exhibit TWIP or TRIP. However, their presence induces additional hardening and enables higher strength and ductility levels. The tendency for an alloy (e.g., steel) to deform by either slip, twinning, or phase transformation depends significantly on the stacking fault energy, microstructure, and level of strain hardening. As the SFE decreases, the plasticity mechanism changes from dislocation glide to dislocation glide in conjunction with twinning and phase transformation (i.e., TRIP). TWIP and TRIP are observed in many alloys including high-Mn TRIP and TWIP steels [17]. These deformation mechanisms and strain hardening behavior must be understood due to their importance in tuning the alloy properties.

As discussed above, various HEAs exhibit TWIP at certain deformation levels and deformation temperatures. TRIP was also observed in some of the developed compositions. A study conducted by Wu on the FCC-HCP Cr<sub>20</sub>Mn<sub>24</sub>Fe<sub>30</sub>Co<sub>20</sub>Ni<sub>6</sub> TRIP alloy and Cr<sub>20</sub>Mn<sub>15</sub>Fe<sub>34</sub>Co<sub>20</sub>Ni<sub>11</sub> TWIP alloy concluded that the TRIP alloy suffered from a lower phase stability due a lower SFE[13][14]. The TWIP composition on the other hand showed a higher SFE, better phase stability, and maintains the FCC phase. In addition to the FCC-HCP TRIP alloys, a unique and interesting FCC-BCC TRIP HEAs have recently been reported for a limited number of compositions. For example, non-equiatomic V<sub>10</sub>Fe<sub>45</sub>Co<sub>30</sub>Cr<sub>10</sub>Ni<sub>5-x</sub>Mn<sub>x</sub> HEA (where x takes the value of 0, 2.5, and 5%) has been shown to exhibit an FCC-BCC TRIP effect at cryogenic

temperatures. By varying the Ni and Mn content, the stacking fault energy (SFE) was altered, and its effect on the resulting deformation mechanism (i.e., slip, twinning, or Transformation) was investigated. The ductility increased with the increase in Mn wt.% at room temperature but decreased at cryogenic temperature. In addition to that, increasing the Mn content to 5% showed an impressive increase in tensile strength. However, the ductility was compromised at cryogenic temperatures due to changes in the SFE to levels not conducive to deformation twinning[11]. The results of the study showed that increasing the Mn from reference composition (0Mn) reduced the SFE. Therefore, at reference composition (0Mn) and room temperature deformation, the resulting SFE was high, which limits deformation to plastic slip. However, at cryogenic temperatures, the SFE was lower, and the deformation was mainly accommodated through a unique FCC to BCC martensitic transformation (TRIP effect) while still maintaining high ductility levels despite the presence of the BCC phase. In addition to temperature, deformation rate also plays a role in dictating the dominant deformation mechanism. For example, changing the deformation rate from quasi-static ( $10e-3/s$ ) to dynamic ( $10e3/s$ ) rate causes a reduction of TRIP and an increase of TWIP at both room and cryogenic temperatures in V10Cr10Fe45Co30Ni5 HEA[16].

As discussed above, TWIP and TRIP are some of the dominating mechanisms that occur during deformation in FCC HEAs and MEAs (medium entropy alloy). These mechanisms lead to excellent mechanical properties under low temperatures. High Mn (Manganese) steel also undergoes the TRIP effect alongside HEAs and MEAs. The understanding of the effect of SFE on the development of TWIP and TRIP has been developed from earlier studies on TRIP/TWIP steels. For example, D.T. Pierce studied the Fe-22/25/28Mn-3Al-3Si system at room temperature [38]. Tensile test showed that the SFE (15, 21, and  $39\text{mJ/m}^2$ , respectively) of the alloys increased dramatically with increasing the Mn content. The range of SFE from 15 to  $39\text{mJ/m}^2$  results in a transition from TRIP to TWIP behavior and an excellent combination of UTS and total elongation. J. Yang et al. designed Fe45Co30Cr10V10Ni5-xMnx (where x is 0%, 0.25, and 5) HEA to investigate the role of Ni and Mn on the Stacking fault energy (SFE) and observe the transformation mechanism. TRIP mechanisms were analyzed by correlating the microstructural evolution and SFE during deformation[17]. J. Yang concluded that the 0Mn HEA at room temperature showed only dislocation glide (i.e., slip). At cryogenic temperature, FCC to BCC martensitic transformation occurred. This

TRIP frequently occurs in austenitic steel and Fe-Co alloys. As Mn content increases, the Gibbs free energy between FCC and HCP phases decrease and the SFE also decrease. With this reduction in SFE, the ductility increased at room temperature but decreased at cryogenic temperature. Compared to the high rate of martensitic Transformation of BCC, at cryogenic temperatures, twins were hardly observed, but HCP transformation increased due to the decrease of SFE by temperature effect. Overall fraction of martensite was higher than that at room temperature. The deformation-induced BCC martensite beneficially contributed to the significant improvement of strain hardening and consequently both strength and ductility [17][38].

When Z. Li et al. [14] developed a new class of Dual Phase (DP)-TRIP-HEA  $\text{Co}_{20}\text{Cr}_{20}\text{Fe}_{34}\text{Mn}_{20}\text{Ni}_6$ , it exhibited a higher UTS and strain hardening ability compared with the equiatomic cantor alloy  $\text{CoCrFeMnNi}$  along with improved mechanical properties. X. Gao, Y. Lu, and J. Liu et al. studied the non-equiatomic FCC HEA  $\text{Cr}_{26}\text{Mn}_{20}\text{Fe}_{20}\text{Co}_{20}\text{Ni}_{14}$  with a comparably low SFE under room temperature and normal strain rate of 0.001/s, and then mechanical properties were compared with the equiatomic  $\text{CoCrFeMnNi}$  HEA which exhibits TWIP at generally cryogenic temperatures. Due to the low SFE in the alloy, the TWIP effect took place at room temperature. The alloy has also shown a high strain hardening exponent of 0.46 and higher ductility than its equiatomic opponent [39].

P. Yu, R. Feng, and J. Du et al. studied the  $\text{FeNiCoCrAl}_{0.36}$  HEA using the density functional theory (DFT) combined with the phonon calculation to estimate the stacking fault energies and temperature-dependent phase stabilities of different structures[40]. The authors found that alloying with Al enhances the metastability of the HEA and has an essential role in the twin formation and the stacking faults. H.-U. Jeong and N. Park investigated the deformation behavior of three medium entropy alloys  $\text{Fe}_{60}(\text{CoCrMnNi})_{40}$ ,  $\text{Fe}_{65}(\text{CoCrMnNi})_{35}$ , and  $\text{Fe}_{70}(\text{CoCrMnNi})_{30}$  to see how the different compositions have different mechanical behavior based on TWIP and TRIP[41]. The alloy having 60% -65% Fe had an excellent ductility while the 70% Fe alloy had high strength. In fact, 60% Fe alloy showed the highest ductility caused by the TWIP, while the TRIP effect was found in the alloy containing 70% Fe giving it the highest strength. An alloy containing 65% Fe exhibited both TRIP and TWIP effects giving this alloy a good combination of strength and ductility.

## Chapter 3. Methodology

### 3.1 Material preparation

A HEA ingot with a non-equiatomic composition of  $V_{10}Fe_{45}Co_{30}Cr_{10}Ni_5$  (at.%) was prepared by arc melting using pure elements (purity >99.5 wt.%). Following casting, the ingot was homogenized at 1200°C for 24hr in an Argon atmosphere. The resulting microstructure following homogenization was characterized using Electron-backscatter diffraction (EBSD). **Fig.3.1a** shows an SEM backscatter image of the grain strain structure. The corresponding grain orientation map is shown in **Fig.3.1b**.

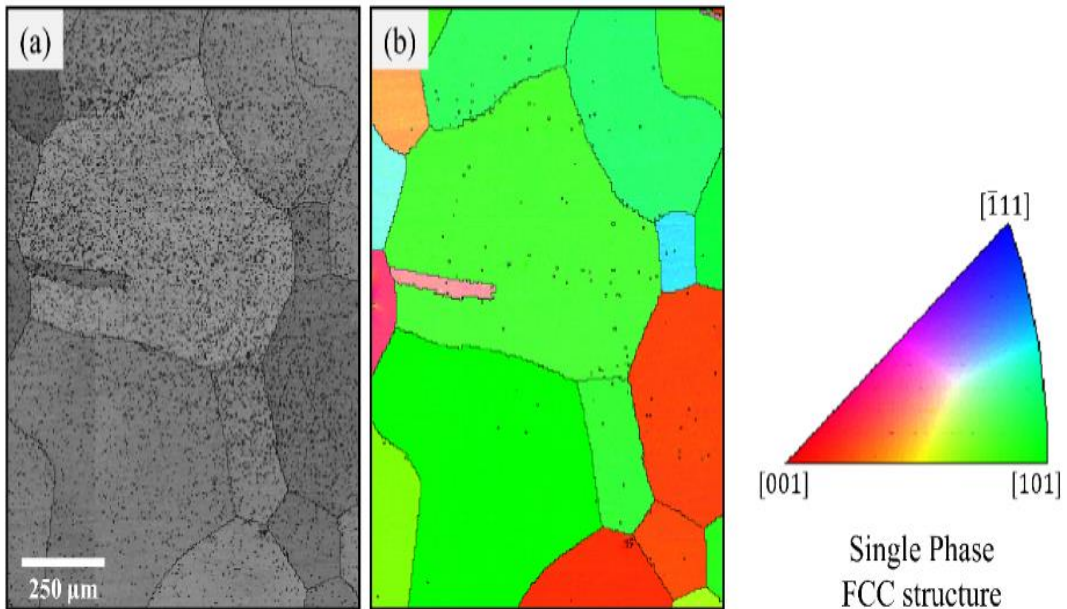


Figure 3.1: (a) SEM backscatter image showing the grain structure of cast material.  
(b) the corresponding grain orientation map

The results highlight a single-phase FCC structure with coarse grains and a wide distribution in grain size. For proper control of grain size, 3 mm thick sheets were machined from the homogenized ingot and subsequently cold rolled to a final thickness of 1.1 mm (i.e., 65.5 % CW). Dog-bone-shaped tensile samples with a gauge length of 8 mm and a cross-section width of 3 mm, and a thickness of 1.1 mm were machined from the rolled sheets. A schematic of the Dog-bone tensile sample is shown in **Fig3.2**. Prior to loading, all samples were heat-treated at 1050°C for 20 minutes, followed by water quenching. To prevent oxidation during the high-temperature solutionizing

treatment, samples were encapsulated in quartz tubes with an inert Ar atmosphere (see Fig 3.3)

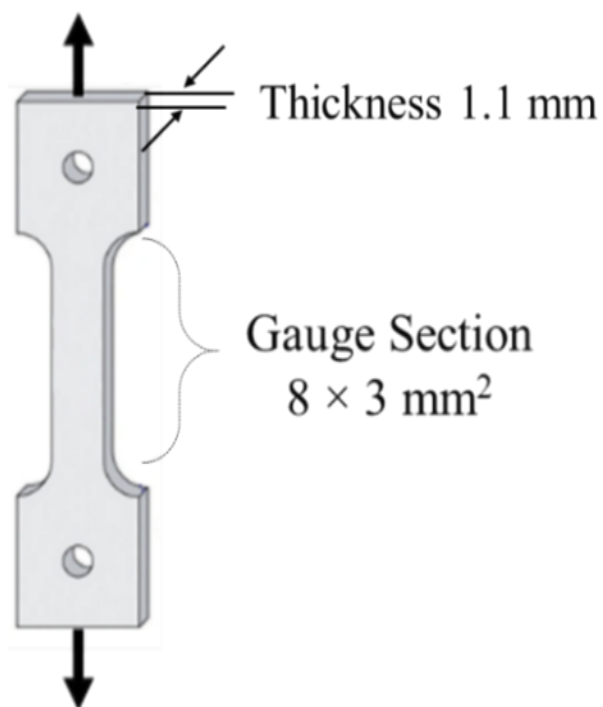


Figure 3.2: Dog-bone-schematic

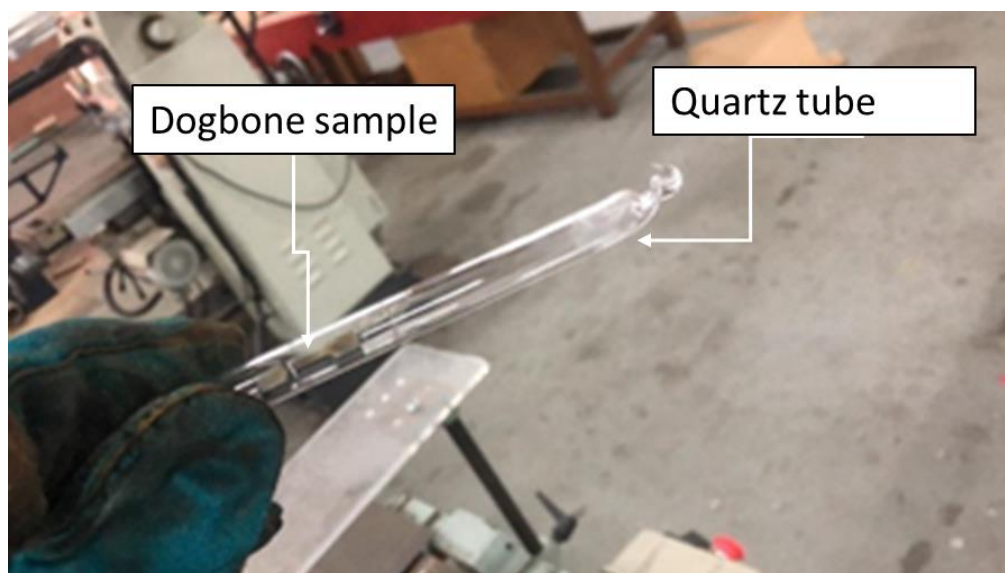


Figure 3.3: encapsulated sample

XRD measurements were conducted following the solution treatment using X'Pert3 Powder X-ray diffractometer (XRD) (PANalytical, UK). The obtained pattern,

shown in **Fig3.4a**, confirms the single-phase FCC structure. Based on the XRD peaks, the calculated lattice parameters are shown in **Table1**.

Table 1:lattice parameter at XRD peaks.

2θ	PEAK	D(hkl)	a
43.6	<111>	2.07	3.58
50.72	<200>	1.79	3.59
75.1	<220>	1.26	3.56
90.7	<311>	1.081	3.58

In addition, the energy dispersive spectroscopy (EDS) analysis, shown in **Fig.3.4c**, highlights the composition homogeneity with no signs of segregation or second phase particles. The resulting composition, which was consistent from multiple areas and samples, is summarized in **Fig. 3.4b**.

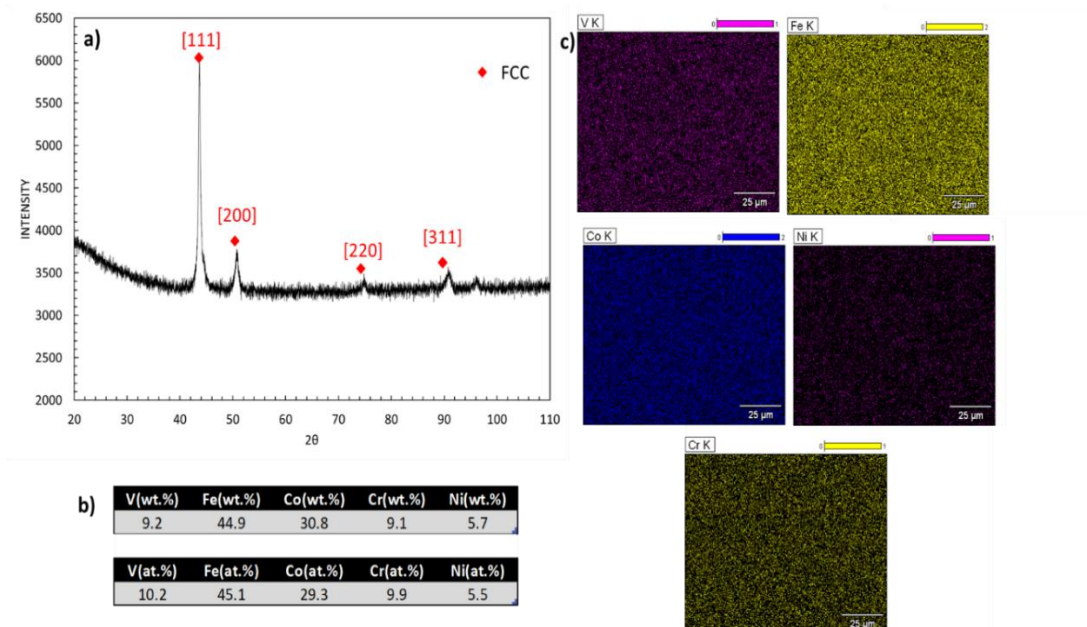


Figure 3.4:(a) XRD Data showing FCC peaks, (b), EDX data confirming the non-equiatomeric composition of the HEA, (c) EDX mapping confirming the homogenous distribution in the material.

### 3.2 Experimental tools

**Digital Image Correlation** Tensile experiments were conducted at various deformation temperatures. Digital image correlation (DIC) was the main tool for strain measurements at room temperature (RT) and elevated deformation temperatures (up to 573K). This full-field, optical, and non-contact technique provides local measures of the displacement field, which can be derived to obtain in-plane strains. DIC works by taking multiple high-resolution images of a sample with a speckle pattern while being deformed. The deformed images collected at the sample's surface are compared to a reference image captured before loading. The correlation process (i.e., calculating local displacements spatially) relies on detecting the motion of the fine speckles applied on the specimen's surface. It is essential to have a random pattern to enable unique and thus trackable features in the region of interest. Also, it is important to ensure the adequate size of speckles with respect to the object being tested. For example, larger objects require bigger speckles than smaller specimens that need a finer speckle pattern. A careful application of a speckle pattern on the AOI (area of interest) is required for the specimens considered in this work. Due to the small area of interest and the considered deformation temperatures, a high-temperature black paint spray with a fine nozzle was used to establish an adequate pattern. The speckle pattern was applied through a series of uniform coats to ensure a random speckle pattern. A representative specimen showing the resulting pattern is shown in Fig 3.5; also, a high-resolution camera in Fig 3.6 was used to capture reference and deformed images.

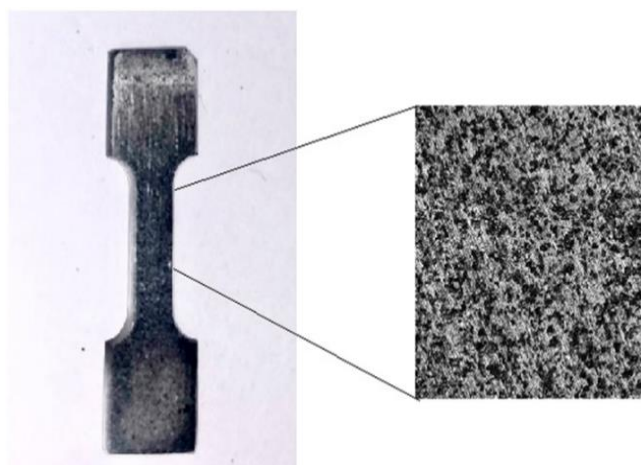


Figure 3.5: Dog bone with speckle pattern (magnified)

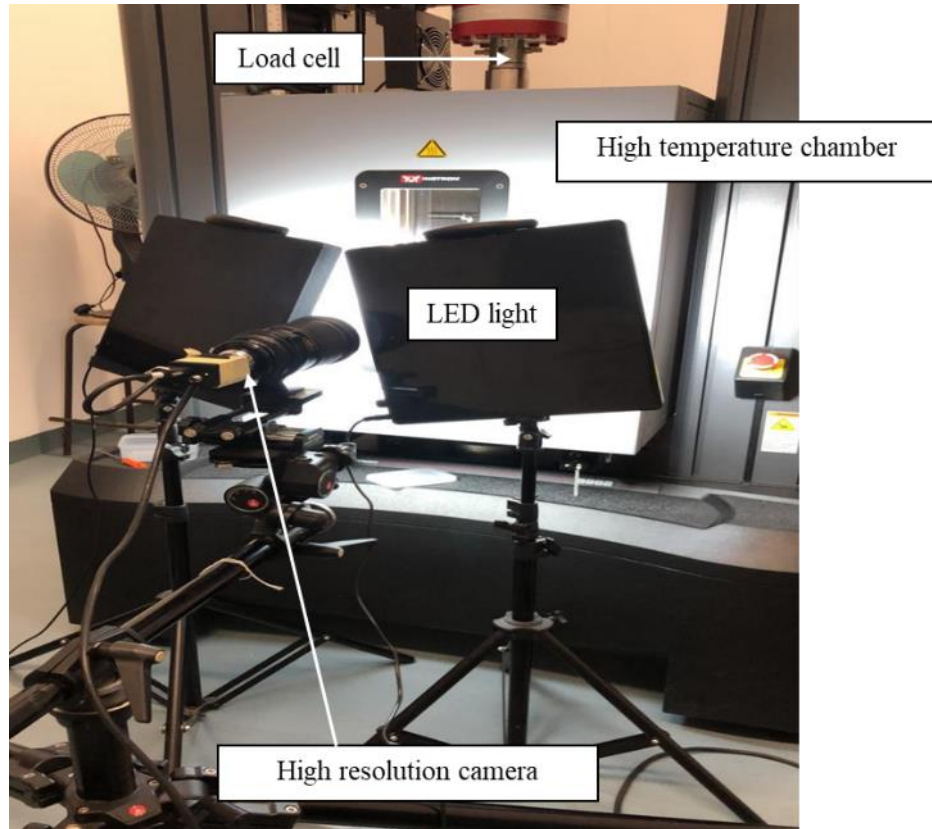


Figure 3.6: Experimental setup

### 3.3 Experimental setup and procedure

Dog-bone tensile specimens of as-cast and cold-rolled V10Cr10Fe45Co30Ni5 were tested using an Instron Universal Testing Machine (UTM) equipped with an environmental chamber at different temperatures and deformation rates. Three different strain rates were considered,  $1.32e^{-3}$  /s, 0.66 /s, and 1.32 /s, the maximum achievable strain rate in the utilized setup. For each strain rate, specimens were tested at room temperature (RT-293 K), cryogenic temperature 77K, and a high temperature of 573K (the maximum attainable temperature for the utilized environmental chamber). For the RT experiments, optical images were captured during deformation using a high-resolution camera connected to VIC-snap with a capture rate of 1 image per 500 ms (milliseconds). VIC-2D commercial software from *correlated solutions*, USA was used to measure the displacement fields and calculate the associated strains. **Fig3.6** shows the experimental setup. Custom grips, shown in **Fig 3.7** were designed and machined to accommodate the tensile samples investigated in this work. Each sample was tightly secured in the fixture with bolts and washers to ensure uniform application of the load with no slippage. During the tests under cryogenic temperature, a box was made from

aluminum to fully submerge the sample along with the fixture in liquid nitrogen (LN), this can be seen in **Fig3.8**.

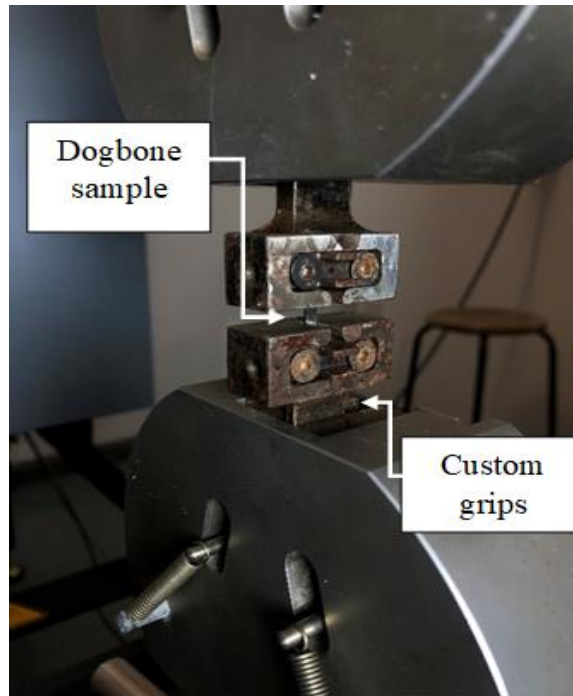


Figure 3.7:Dog bone grips

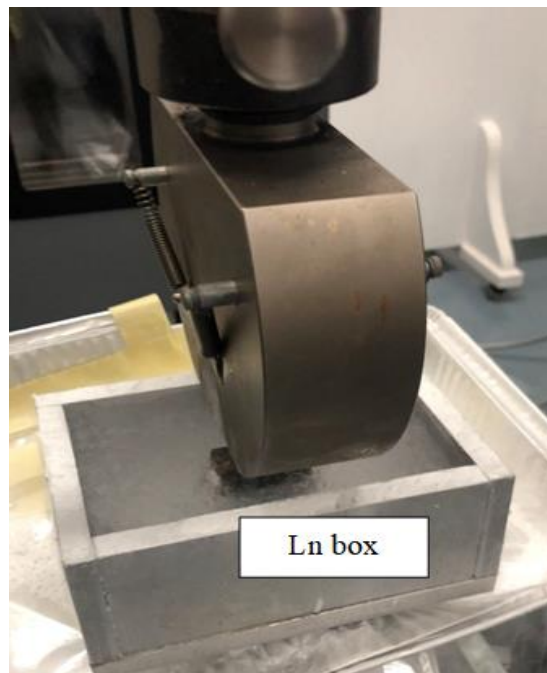


Figure 3.8:aluminum box for experiments in LN

## Chapter 4. Results

Previous works on polycrystalline  $V_{10}Fe_{45}Co_{30}Cr_{10}Ni_5$  have reported TWIP in specimens deformed at RT and TRIP at cryogenic loading temperatures. This work will consider the polycrystalline  $V_{10}Fe_{45}Co_{30}Cr_{10}Ni_5$  at different deformation temperatures and strain rates, ranging from 77K up to 573.15K and  $1.32 \times 10^{-3} /s$ ,  $0.66 /s$ ,  $1.32/s$  respectively. In this section, deformation results under different strain rates and temperatures will be discussed, alongside the SEM image of the sample's fractured surfaces.

### 4.1 Tensile properties in as-cast microstructure

Initially, the tensile properties were evaluated prior to any microstructural optimization through rolling (i.e., cast and solutionized only –No cold rolling). The considered deformation temperatures and strain rates are shown in **Table 2**. Three-four tensile specimens were tested for each condition. **Fig 4.1** shows representative stress-displacement curves for the considered conditions. At RT and slow strain rate of  $1.32e-3/s$ , it can be seen that this sample had low strength but high ductility. At a similar strain rate but  $-196^{\circ}C$  deformation temperature (LN), the sample achieved a higher strength with the ductility being much lower than the control sample. For the higher deformations rates, the specimens achieved high strength but very low ductility compared with the control sample (i.e., RT and slow deformation rate). This response is rather surprising based on available literature. In addition, it should be pointed out that a significant specimen-specimen variation was observed. Based on the collected microstructural analysis. The large variation in response seen in **Fig. 4.1** was attributed to the heterogeneity in grain size (i.e., lack of optimized microstructure). The material was cold-rolled and annealed to improve the microstructural homogeneity and reduce variation in mechanical properties.

Table 2: Testing Strain rates and temperatures

STRAIN RATES	TEMP
LSR ( $1.32e-3/s$ )	RT ( $25^{\circ}C/298.15K$ )
HSR ( $0.66/s$ )	LN ( $-196^{\circ}C/77K$ )
UHSR ( $1.32/s$ )	HT ( $300^{\circ}C/573.15K$ )

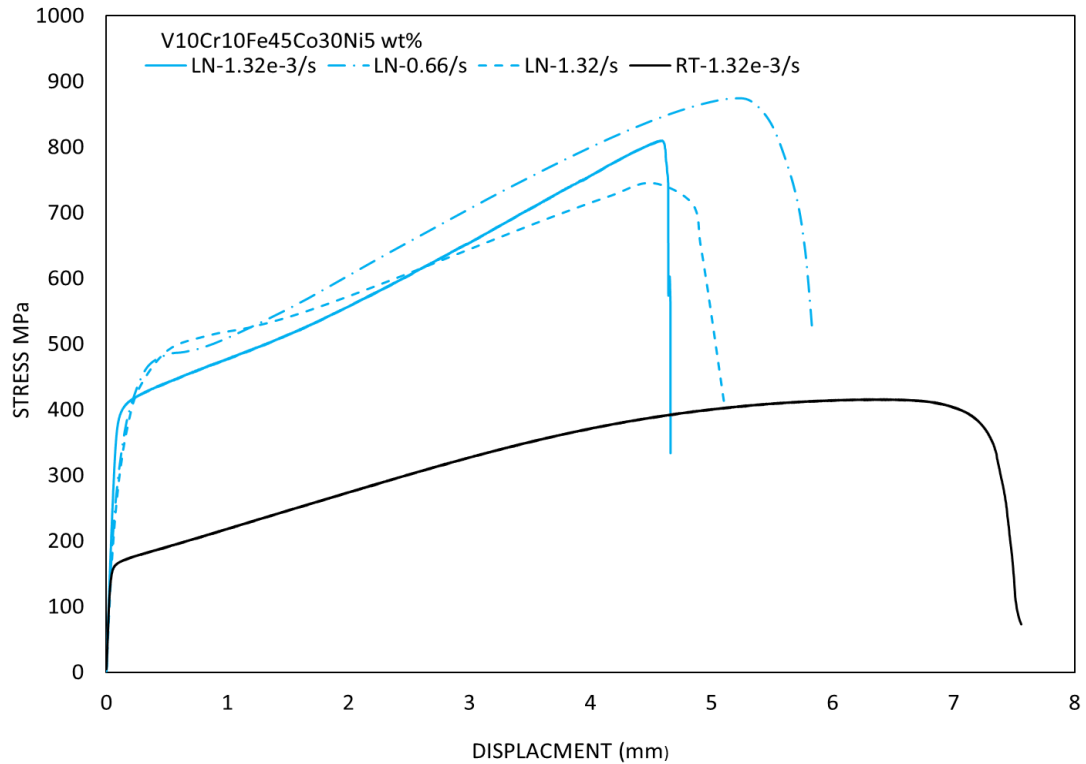


Figure 4.1: Preliminary Stress-Strain curves

#### 4.2 Tensile properties – optimized microstructure

To address the significant variation in mechanical properties in the as-cast conditions, rolled and annealed specimens were considered. The rolling and heat treatment processes help reduce the grain size, which was very coarse in the cast structure, and grain size distribution, which was very wide, as described above in **Fig 4.1**. The full details of the rolling process and subsequent heat treatment and specimen preparation were detailed in **Section 3.1** of this report. Three different deformation temperatures and strain rates were considered. For each condition, three different specimens were loaded in tension. Representative engineering stress-strain curves are shown in **Fig 4.2**, one for each of the considered deformation temperatures and strain rates. To further understand the response of the material at different strain rates and temperatures, one should first look at the response of the material at room temperature (RT). The results clearly indicate that at (RT), the highest ductility was achieved at the slowest strain rate of  $1.32 \times 10^{-3} /s$ . In all of the considered specimens, increasing the deformation strain rate to either 0.66 /s and 1.32/s resulted in reduced ductility. When comparing the yield strength (0.2% offset) obtained from the different deformation rates at Room Temperature (RT), a linear correlation between the deformation rate and

the resulting yield strength was not observed. The highest yield strength was measured at the intermediate rate (0.66/s) with slower ( $1.32 \times 10^{-3}$  /s) and faster rates (1.32/s), resulting in lower yield strengths. For the ultimate tensile strength (UTM), the attained strength levels did not differ significantly at different deformation rates (all RT). **Tables 3 and 4** provide a summary of all the calculated magnitudes.

Decreasing the deformation temperature to 77K (blue curves) resulted in a significant increase in both; strength and ductility. The effect was more pronounced at the slow deformation rate of  $1.32 \times 10^{-3}$  /s which resulted in the highest strength levels in all of the considered conditions with superior ductility. Similar to the results obtained at RT, the highest yield strength at 77K was again obtained at the intermediate deformation strain rate of 0.66/s. However, as the ductility differed significantly at 77K compared to the RT specimens, a pronounced difference in the UTS was also observed. Aided by the high ductility and hardening levels at  $1.32 \times 10^{-3}$  /s strain rate, the UTS reached noticeably higher magnitudes (an impressive 1.2 GPa with ductility exceeding 50%).

Increasing the deformation temperature to 300°C (red curves in Fig. 4.2) resulted in enhanced ductility levels; however, this was accompanied by a significant strength reduction. Due to the limitation in the number of available specimens, only two deformation rates were considered at this temperature. By increasing the deformation strain rate, the expected, and consistent across all temperatures, reduction in ductility was observed. However, and unlike the results obtained at RT and 77K, both the yield and UTS dropped compared to the slow strain rate results.

**Tables 3 and 4** summarizes the mechanical properties of the studied HEA at all temperatures and strain rates. It can be seen from the table, the sample that deformed under cryogenic temperature and a strain rate of  $1.32 \times 10^{-3}$  /s gave the highest Ultimate Tensile strength (UTS) of around 1225 MPa and ductility of 62.2 %, while samples deformed under high temperatures 300 °C and strain rate of  $1.32 \times 10^{-3}$  /sgave the highest ductility of 71.5%. To further highlight the effect of deformation temperature and strain rate on the obtained mechanical properties, the room temperature, and slow strain rate were used as control conditions and the relative change in strength and ductility were calculated. The results are presented in the last four columns in **Table 4**.

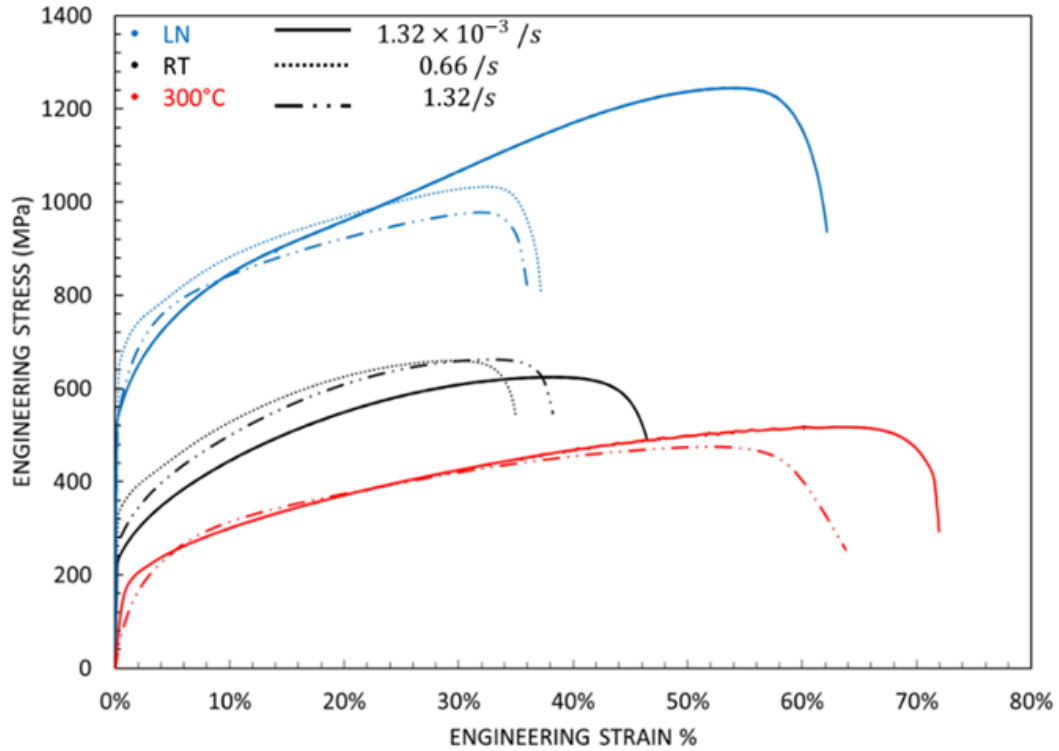


Figure 4.2: Engineering stress-strain curves

The highest increase in strength occurred at LN deformation (98.3% increase), while the largest reduction in strength was obtained at 300°C and 1.32/s deformation strain rate. It is also worth noting that the strength decreased as the strain rate changed at LN and 300°C on the other hand, the strength at Room Temperature (RT) increased by 4.6% when the strain rate was increased from  $1.32 \times 10^{-3} /s$  to  $0.66 /s$ , and it also increased by 5.1% when the strain rate was increased from  $1.32 \times 10^{-3} /s$  to  $1.32 /s$ .

Table 3:  $V_{10}Fe_{45}Co_{30}Cr_{10}Ni_5$  mechanical properties

Label	Temperature	Ductility %	Change in strength due to temp change	Change in ductility due to temp change	Change in strength due to rate change	Change in ductility due to rate change
SLOW-RT	RT	$47.6 \pm 2.8$	REF-TEMP	REF-TEMP		
FAST-RT	RT	$35.5 \pm 0.2$	REF-TEMP	REF-TEMP	4.6%	-25.4%
VERY-FAST-RT	RT	$40 \pm 1.5$	REF-TEMP	REF-TEMP	5.1%	-16.5%
SLOW-LN	LN	$62.2 \pm 0.085$	98.3	30.6		
FAST-LN	LN	$34.5 \pm 2.9$	57.9	-3	-16.6%	-44.58%
VERY-FAST-LN	LN	$35 \pm 2$	53.3	-11.9	-18.6%	-43.7%
SLOW-300°C	300°C	$71.5 \pm 4.4$	-16.03	50.3		
VERY-FAST-300°C	300°C	$65.4 \pm 3.5$	-23.8	64.5	-4.5%	-8.6%

Table 4: V10Fe45Co30Cr10Ni5 mechanical properties

LABLE	TEMPERATURE	DEFORMATIN STRAIN RATE	Yield Strength (MPa)	UTS (MPa)
SLOW-RT	RT	1.32e-3/s	245.7 ± 15.4	617.5 ± 21.9
FAST-RT	RT	0.66/s	335.1 ± 1.5	646.02 ± 19.08
VERY-FAST-RT	RT	1.32/s	287.6 ± 37.7	649.6 ± 14.6
SLOW-LN	LN	1.32e-3/s	535.8 ± 18.1	1224.8 ± 29.06
FAST-LN	LN	0.66/s	593.2 ± 54.9	1020.5 ± 16.3
VERY-FAST-LN	LN	1.32/s	577.7 ± 30.9	995.9 ± 54.5
SLOW-300°C	300°C	1.32e-3/s	143.3 ± 51.6	518.5 ± 10.6
VERY-FAST-300°C	300°C	1.32/s	82.4 ± 49.1	494.9 ± 28.4

### 4.3 Crystal structure-observation of TRIP effect

To observe the development of TRIP in the investigated specimens (FCC-BCC) phase transformation, XRD data was collected from all deformed samples. **Fig4.3 and Fig 4.4** shows the XRD pattern collected from a representative specimen prior to loading (i.e., rolled and solution heat treated). The dominant crystal structure for the material under such condition is FCC as noted by the marked peaks in **Fig4.3**. However, and unlike the structure before rolling, a single BCC peak appears in the patterns which points to the presence of some regions with BCC structure. Further optimization of the solution heat treatment, higher temperature or longer time, can help reduce the secondary phase. However, this was not conducted in the current work and is left for future efforts.

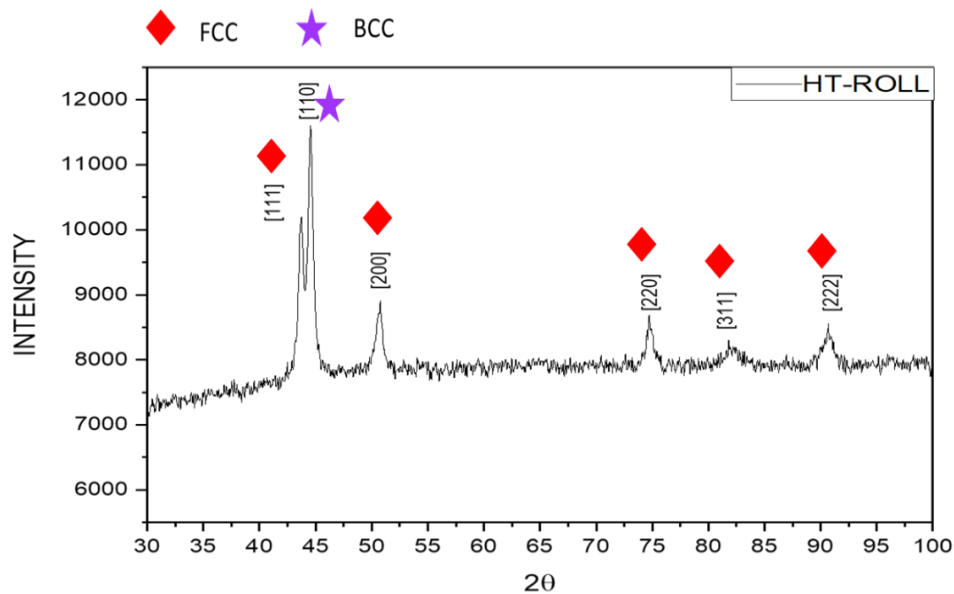


Figure 4.3: XRD of rolled and solution treated specimen

All deformed specimens were investigated following fracture by collecting XRD spectrum from a region within the gauge section and close to the fracture point. The patterns obtained from all specimens deformed at either RT or 300 °C do not point to any phase transformation. This can be observed by noting the similarity between the XRD patterns before (**Fig. 4.3**) and after deformation. However, although XRD can be used to detect TRIP, it should be emphasized here that it does allow for the detection of twinning (TWIP) as this deformation mechanism does not alter the crystal structure. As for the specimens deformed at cryogenic temperature, the XRD patterns point to significant phase transformation and almost complete elimination of the original FCC structure. This can be observed as all the FCC peaks disappeared and additional BCC peaks, [200] and [211], became very visible in the collected diffraction data. The occurrence of TRIP in these samples gave rise to strength and ductility levels, as it can be seen in the stress-strain curves shown in **Fig. 4.2**

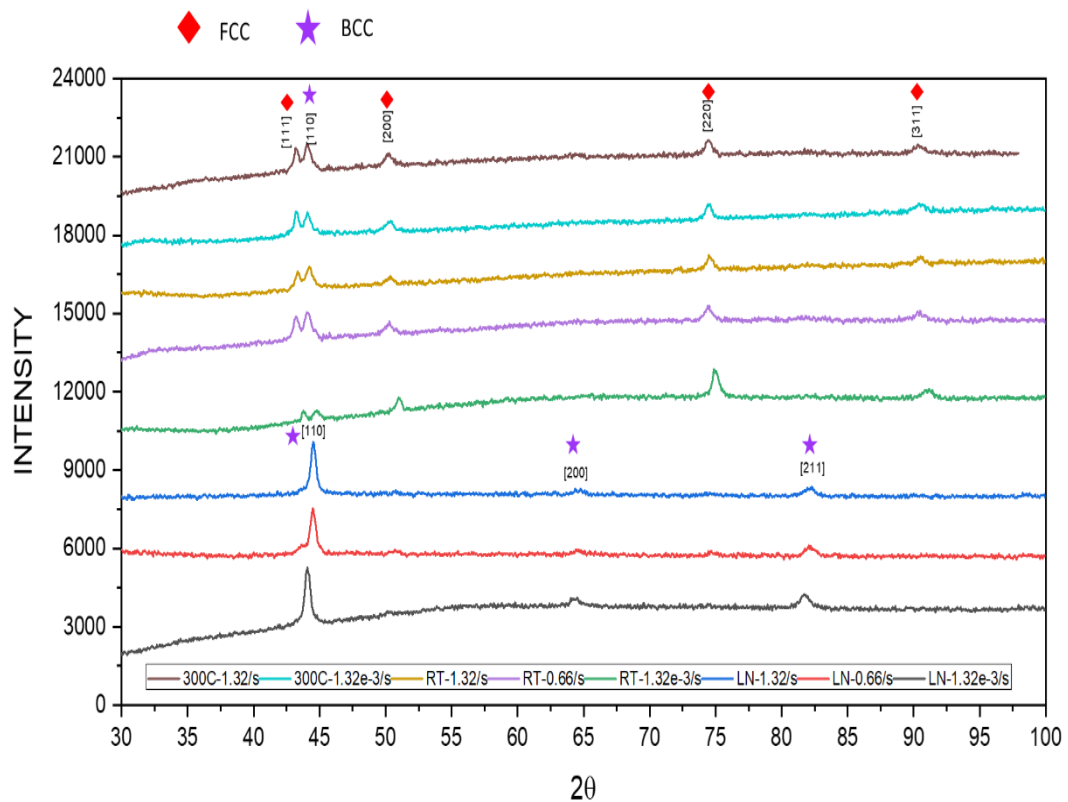


Figure 4.4: XRD of deformed samples at different testing conditions

#### 4.4 Strain rate sensitivity and hardening response

In order to further quantify the strain rate sensitivity for all the considered deformation conditions, the strain rate sensitivity (SRS) parameter( $m$ ) was calculated using the Equation below.

$$m = \frac{\partial \log(\sigma)}{\partial \log(\dot{\epsilon})} \quad (9)$$

where  $\sigma$  is the true stress, and  $\dot{\epsilon}$  is the strain rate[42].

The results obtained from all the considered temperatures and strain rates are presented in **Table 5**. The SRS parameter  $m$  decreases as the temperature decreased from room temperature to cryogenic temperatures (LN), which indicates a lower strain sensitivity at the cryogenic temperature. The lowest strain rate sensitivity was calculated at 300°C between  $1.32 \times 10^{-3} /s$ – $1.32/s$  and the highest value for  $m$  (i.e., pointing to higher strain rate sensitivity) was obtained at room temperature between  $1.32 \times 10^{-3} /s$ – $0.66/s$ . The SRS parameter  $m$  for samples tested at 77K are lower than those tested at Room Temperature (RT). Recent work on the Cantor alloy, FeMnCoCrNi, has also shown a reduction in SRS  $m$  parameter at cryogenic temperatures due to the activation of deformation twinning (TWIP) [43]. The considered V10Cr10Fe45Co30Ni5 alloy also exhibits similar response which is potentially associated with the activation of phase transformation (TRIP) as will be shown later in this section.

Table 5: Variation of strain rate sensitivity  $m$  with temperature.

TEMPERATURE	strain rate	SRS , $m$
RT		
	1.32e-3/s - 0.66/s	0.05
	1.32e-3/s - 1.32/s	0.023
LN		
	1.32e-3/s - 0.66/s	0.017
	1.32e-3/s - 1.32/s	0.011
300°C		
	1.32e-3/s - 1.32/s	-0.08

Strain hardening develops in the material due to plastic strain accumulation. Various aspects influence this phenomenon, including dislocation multiplication and dislocation interface interaction (e.g., grain boundaries and phase boundaries). For example, the TWIP effect introduces additional interfaces (i.e., twin boundaries) that

act as obstacles for dislocation motion, increasing strength and hardening levels. A similar effect takes place in the case of TRIP due to the introduction of phase boundaries [44]. As the investigated material in this study exhibits TWIP and TRIP effects, depending on the deformation temperature, quantifying the hardening level for the different considered conditions is extremely important. The hardening response of the investigated samples can be better quantified by calculating the material hardening rates  $d\sigma/d\varepsilon$ . This calculation is typically conducted using the true stress and strain quantities. For all the considered cases, the true stresses and strains were calculated from their corresponding engineering magnitudes using the following equations, which are valid up to the onset of necking or up to the tensile strength in the engineering stress-strain curve:

$$\text{True strain} = \ln(1 + \text{engineering strain}) \quad (10)$$

$$\text{True stress} = (\text{engineering stress}) * (1 + \text{engineering strain}) \quad (11)$$

$$\text{Strain Hardening} = \frac{d\sigma}{d\varepsilon} \quad (12)$$

In general, the strain hardening rate curve shows four different stages throughout the deformation history. **STAGE I:** This stage of strain hardening is known as easy glide, because large amounts of strain can accumulate without much strain hardening. This stage starts directly after yielding and is usually characterized by a slow decrease in the hardening rate. Researchers believe that the main causes for this stage behavior is due to the development of slip systems and elasto-plastic transition in the deformed crystals. **STAGE II:** This stage is reported to occur after plastic straining and is primarily attributed to the increase and dominance of deformation-induced twinning activities over dislocation slip[45]. At this stage, it is observed that the reduction in hardening remains constant up to certain level and a plateau forms. Subsequent strain hardening is induced by twinning in FCC alloys under deformation. The presence of this stage is a clear indication of TWIP and/or TRIP effects while its absence points, to slip dominated response. The increase in hardening rates is attributed to reduction in the slip length due to the additional interfaces generated by TWIP/TRIP. This response is similar to the Hall-Petch effect associated with grain boundary strengthening. **STAGE III:** This stage can be distinguished by the breakdown of the constant

hardening rate observed in Stage II due to activation of cross-slip processes as a dynamic recovery mechanism. The stress and strain levels needed to move from stage II to stage III were found to be inversely dependent on the SFE and temperature. Alloys with higher SFE do not show this stage, e.g., aluminum and copper. **STAGE IV:** in this stage is reached when the hardening rate is saturated and reaches a finite value. For high SFE FCC alloys this value is zero. It has been suggested that activation of a secondary twinning system further reduces slip lengths and causes additional hardening. [46][47].

**Figs 4.5, 4.6, and 4.7** show the true stress-strain curves with the corresponding strain hardening rates for all the considered cases. Clear differences between the considered cases can be observed. **Fig 4.5 (right)** shows the strain hardening rate for the RT specimens at  $1.32 \times 10^{-3} /s$ ,  $0.66 /s$ , and  $1.32/s$  deformation strain rates. For the  $1.32 \times 10^{-3} /s$  and  $1.32/s$  strain rates, (Stages I and IV) are present. The absence of (Stages II and III) is most probably indicative of the lack of mechanical twinning and cross slip during deformation at this deformation temperature[48]. At  $0.66 /s$ , stages I, II and IV are present. The observed increase in strain hardening rate at stage II is due to the formation of twins (i.e., TWIP effect). In **Fig4.6(right)**, the four stages appear at  $1.32 \times 10^{-3} /s$  and at  $0.66 /s$  and stages I, III, and IV at  $1.32/s$  for deformation under cryogenic temperatures (LN). A typical strain hardening curve of TWIP/TRIP alloys was achieved in which the curve displays a steady plateau in the early stages (10%-20% true strain). A typical TWIP/TRIP alloy shows an increase in the hardening rate from the early stages to intermediate stages in which the strain hardening curve increases to reach the maximum value in the intermediate stage as seen in **Fig 4.6(right, black)**[49]. However, and based on literature [4][50][43][51], TRIP is more likely in these cases. However, EBSD data is required to confirm this. In **Fig 4.7 (right)**, stages I, III and IV at  $1.32 \times 10^{-3} /s$  and  $1.32/s$  in deformation at high temperature (573K). The point of intersection between stress-strain and strain hardening curves corresponds to the point at which plastic instability occurs, after which necking occurs in the samples. Neither TRIP nor TWIP are expected at this deformation temperature. However, EBSD data is required to unambiguously confirm this.

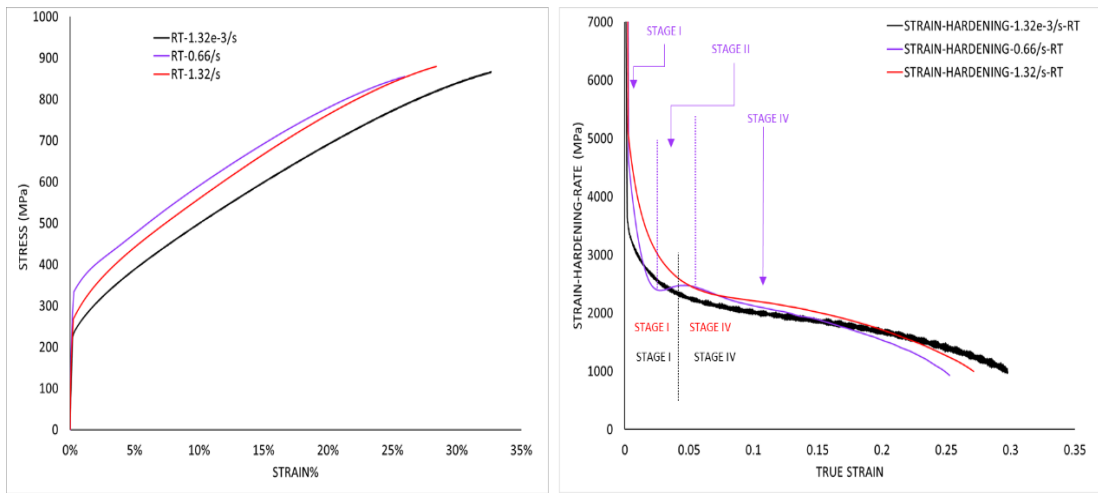


Figure 4.5: True stress-strain curves (left), Strain Hardening (right)-RT

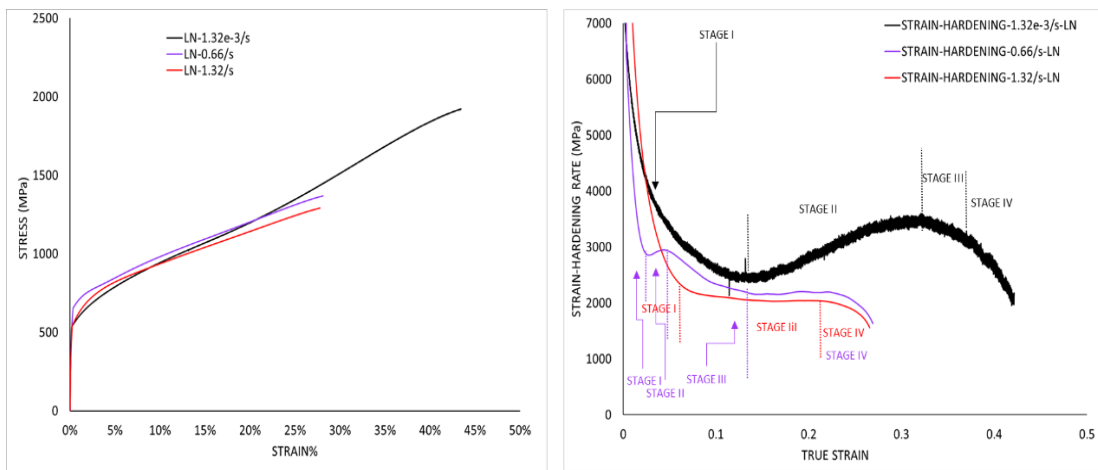


Figure 4.6: True stress-strain curves (left), Strain Hardening (right)-LN

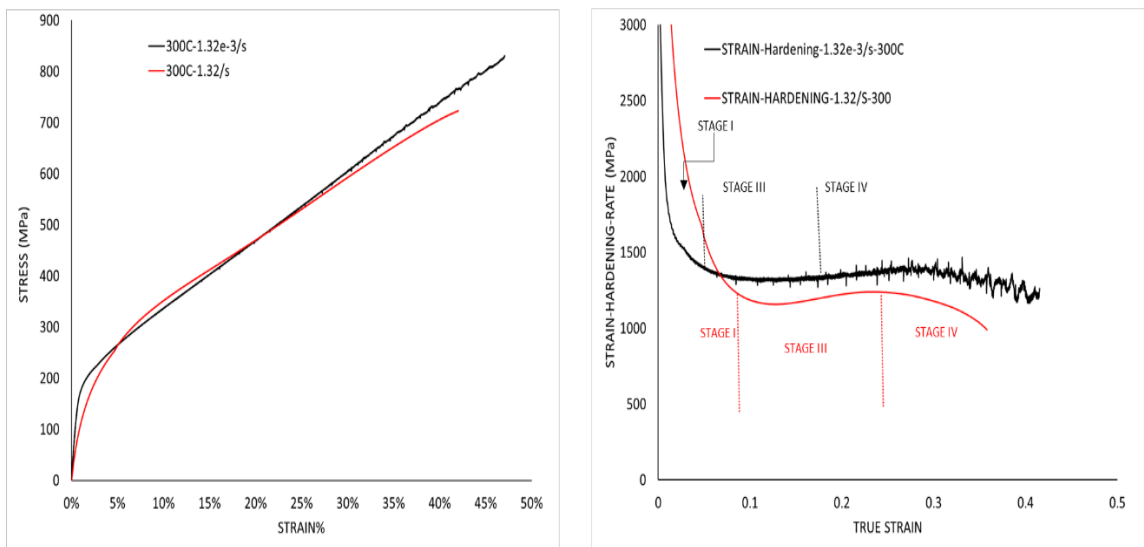


Figure 4.7: True stress-strain curves (left), Strain Hardening (right)-300°C

#### 4.5 Fracture surface analysis

The Scanning Electron Microscope (SEM) was used to observe the fracture surfaces of all the considered deformation conditions. Representative SEM images, all collected at the same magnification, are shown in **Figs. 4.8-4.10** for the RT, LN, and 300 °C deformation temperatures, respectively. Ductile dimples can be observed at all temperatures and strain rates. However, there are some flat regions marked with arrows in **Figs 4.8 a, 4.8c, 4.10a and 4.10b**; this indicates failure, which may be due to the grain boundary sliding at these conditions.

For the RT deformed specimens (**Figs4.8 a, b and c**), ductile dimples can be seen in all the samples. However, at 1.32e-3/s and 1.32/s deformation rates, the features look less fibrous and sharper than the image taken at 0.66/s deformation rate. For the LN deformed specimens (**Figs4.9 a, b and c**), compared with the images taken at RT. It can be seen that these samples contain more dimples, which indicates a higher ductility, and a much more fibrous appearance indicating that these samples exhibited high strengths. This can be clearly observed by comparing **Fig. 4.9 a(LN)** to **Fig. 4.8 a (RT)**. The strength and ductility levels at LN were significantly higher which is consistent with the observations made on the fracture surfaces. **Figs4.10a and b** represents the SEM fractography of the samples deformed at 300°C. These samples also contain ductile dimples, but they lack the dull and fibrous appearance. Which indicates that the samples did not show high strengths compared samples deformed on other temperatures. The relationship between the dull and fibrous appearance with the strength can be observed through **Fig 4.2**.

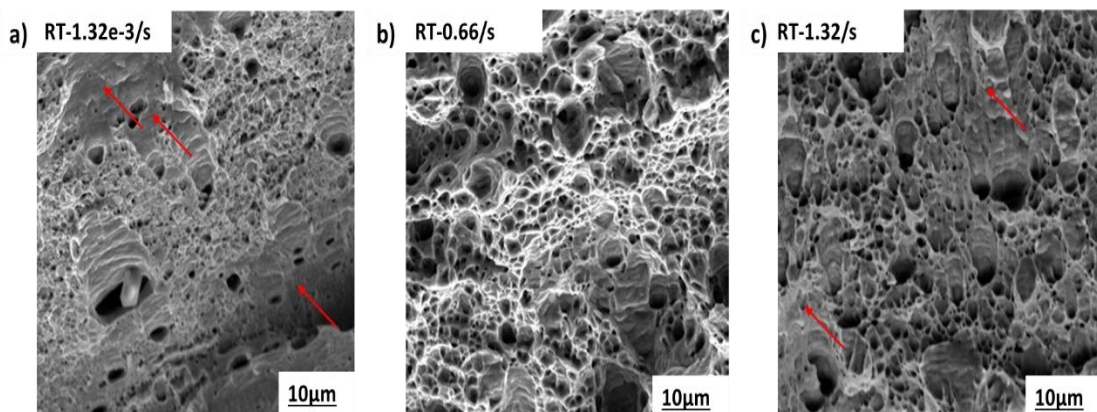


Figure 4.8:Fracture surfaces of tensile specimens at RT a) 1.32e-3/s, b)0.66/s, c)1.32/s

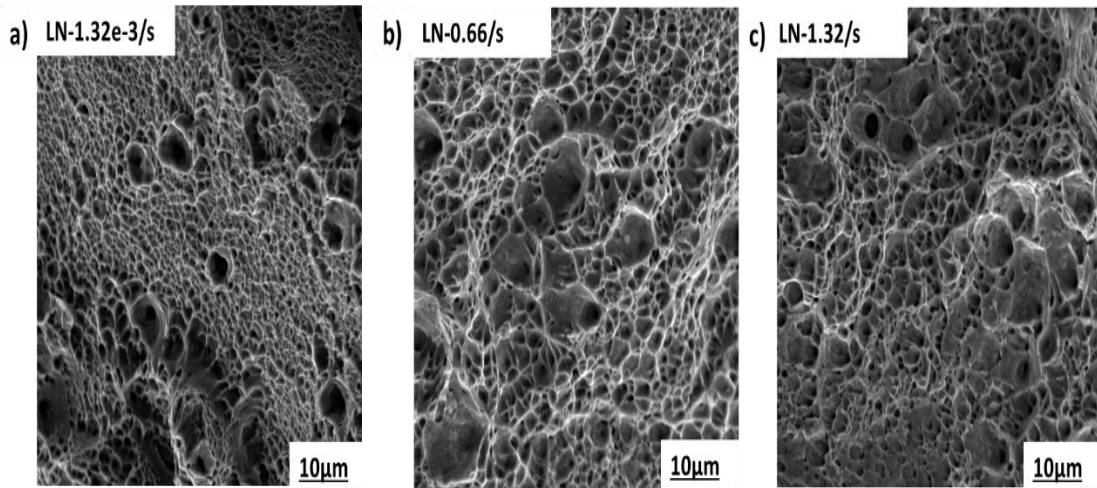


Figure 4.9: Fracture surfaces of tensile specimens at LN a)  $1.32e-3/s$ , b)  $0.66/s$ , c)  $1.32/s$

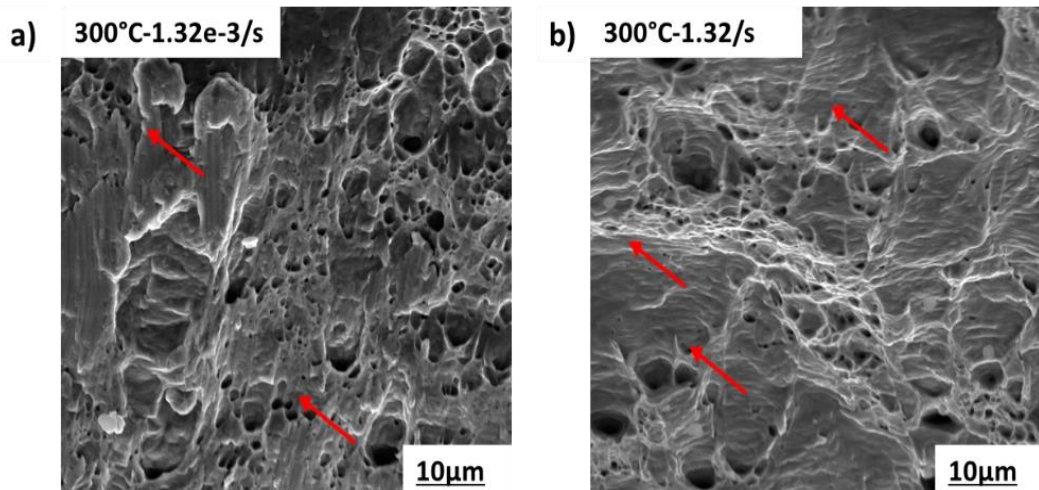


Figure 4.10: Fracture surfaces of tensile specimens at 300°C a)  $1.32e-3/s$ , b)  $1.32/s$

## 4.6 Modelling

**4.6.1 J-C model.** As discussed above, the Johnson-cook model has been widely used to calculate the flow stress due to its relative simplicity and fast calculation speed. The model was first introduced by Johnson and cook in 1983 to describe the relationship between stress and strain in metals under high strain rates, large deformations, and high temperatures. The flow stress takes the following form:

$$\sigma = (A + B\varepsilon^n)(1 + C \ln \dot{\varepsilon}^*)(1 - T^{*m}) \quad (13)$$

where

$$T^* = \frac{T - T_r}{T_m - T_r} \quad (14)$$

$$\dot{\varepsilon}^* = \frac{\dot{\varepsilon}}{\dot{\varepsilon}_r} \quad (15)$$

$\sigma$  equivalent true stress,  $\varepsilon$  equivalent true strain,  $\dot{\varepsilon}$  strain rate,  $\dot{\varepsilon}_r$  reference strain rate,  $T_m$  melting point,  $T_r$  reference temp,  $A$  is the yield stress for the reference deformation conditions,  $B$  is the strain hardening constant,  $n$  is the strain hardening exponent,  $C$  is the strain rate strengthening coefficient, and  $m$  is the thermal softening coefficient. To calibrate the model parameters, stress-strain data at different temperatures and strain rates is required. The following subsection details the steps undertaken to determine the model parameters for the investigated material in this work.

**4.6.1.1 Fitting J-C model parameter** Determination of Material Constants  $B$  and  $n$  When the deformation temperature is  $T = T_r = 77 \text{ K}$  and the deformation strain rate is  $\dot{\varepsilon} = \dot{\varepsilon}_r = 1.32 \times 10^{-3} \text{ s}^{-1}$ , the equation above Eq13 is modified as follows:

$$\sigma = (A + B\varepsilon^n) \quad (16)$$

Here, thermal softening effects and the influence of strain rate strengthening are neglected. By rearranging and taking the natural log on both sides, the previous Equation Eq16 is modified to:

$$\ln(\sigma - A) = (n \ln \varepsilon) + (\ln B) \quad (17)$$

By substituting the values of the equivalent stress and equivalent strain at reference conditions in the above Equation (Eq17), a linear plot can be generated between  $\ln \varepsilon$  (x-axis) and  $\ln(\sigma - A)$  (y-axis). The magnitude of  $A$  was determined to be

500 MPa, which is the yield point of the material at reference temperature and strain rate. In the resulting graph, the slope of the linear line represents constant **n** while **B** can be determined from the Y-intercept. As shown in **Fig. 4.11**, **n** was found to be 0.7 and **B** = 2100 MPa.

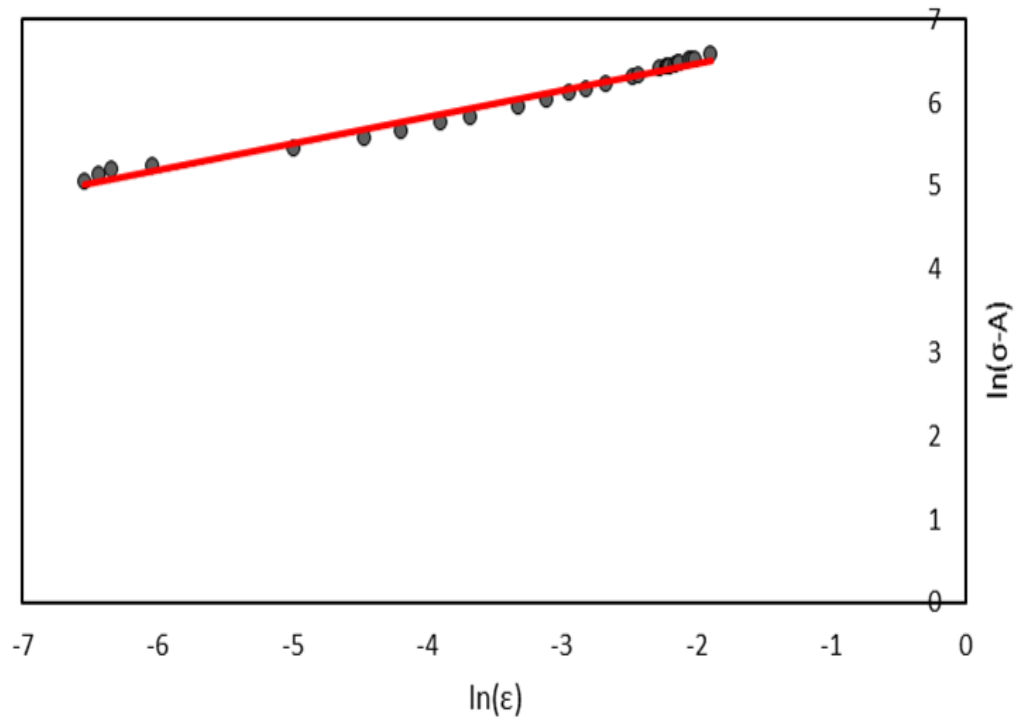


Figure 4.11: **n** and **B** curve fitting

**Determination of Material Constants C** When the deformation temperature is  $T = T_r = 77$  K, the J-C model equation above Eq13 is modified as follows:

$$\sigma = (A + B\epsilon^n)(1 + C \ln \dot{\epsilon}^*) \quad (18)$$

the influences of thermal softening effects are ignored in this form. Rearranging the Equation **Eq18** above will result in the following form:

$$\sigma / (A + B\epsilon^n) = (1 + C \ln \dot{\epsilon}^*) \quad (19)$$

By substituting the values of equivalent true stress and strain, **A**, **B**, and **n** at different strain rates, the Equation above **19** will result in a number of points that will produce the value of **C** as seen in **Fig 4.12**. By curve fitting to the slope, the value of **C** was determined as  $C \approx 0.001$ .

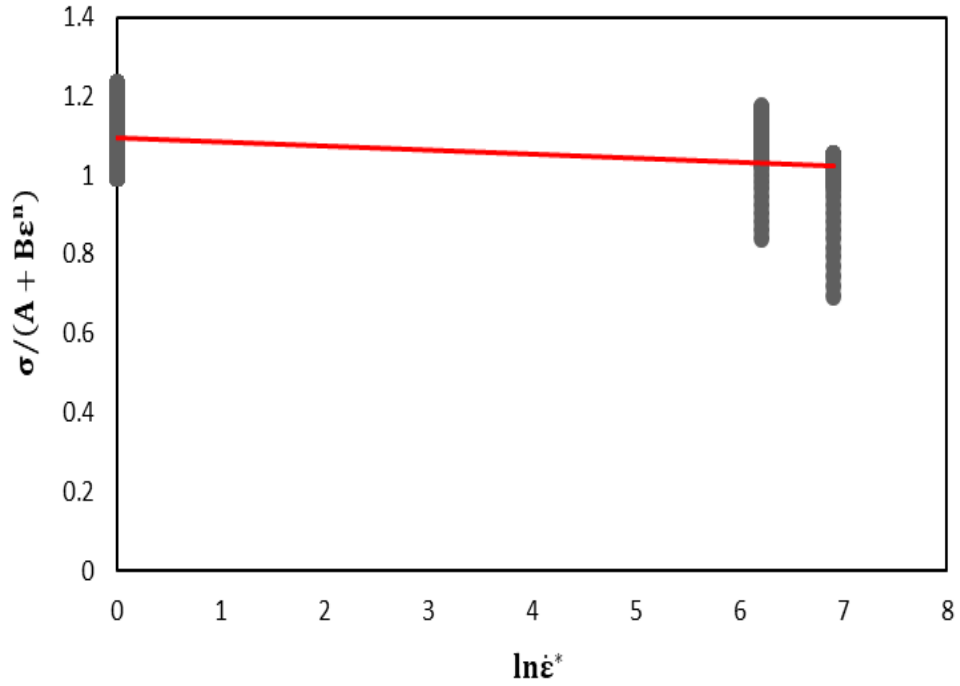


Figure 4.12: C curve fitting

**Determination of Material Constant m** When the deformation strain rate is  $\dot{\epsilon} = \dot{\epsilon}_r = 1.32e-3/s$ , the equation above (Eq13) is modified as follows:

$$\sigma = (A + B\epsilon^n)(1 - T^{*m}) \quad (20)$$

Here, the influences of strain rate strengthening are neglected. Rearranging the Equation **Eq20** above will result in the following form:

$$1 - \left( \frac{\sigma}{(A + B\epsilon^n)} \right) = (T^{*m}) \quad (21)$$

Taking the natural log of the Equation on both sides results in the following:

$$\ln \left[ 1 - \left( \frac{\sigma}{(A + B\epsilon^n)} \right) \right] = m \ln T^* \quad (22)$$

By substituting the values of the equivalent true stress, true strain, **A**, **B**, and **n** at different temperatures, the Equation above Eq22 will result in a number of points that will produce the value of **m** through curve fitting as seen in Fig 4.13. The slope of the curve representing **m** was found to be  $m \approx 0.393$ .

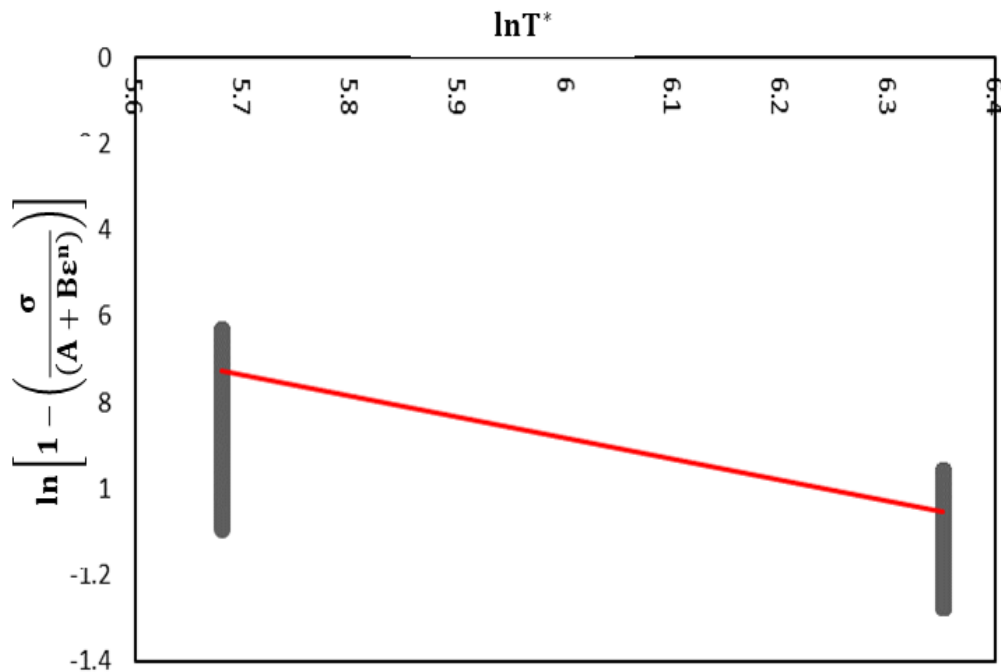


Figure 4.13:m curve fitting

**4.6.1.2 J-C model results** Following the procedure describes above; all the relevant J-C model parameters were established for the V10Cr10Fe45Co30Ni5 alloy investigated in this work. Table 5 provides a list of all model parameters along with their fitted magnitudes.

Table 6: J-C model parameters

<b>Ref temp</b>	<b>77K</b>
<b>Ref strain rate</b>	<b>1.32e-3/s</b>
<b>A</b>	<b>500</b>
<b>B</b>	<b>2100</b>
<b>n</b>	<b>0.7</b>
<b>C</b>	<b>0.001</b>
<b>m</b>	<b>0.393</b>

**Fig 4.14** through **Fig 4.16** demonstrate the Johnson-cook model along with the experimental true stress-strain curves at different temperatures and strain rates. **Fig 4.14** shows the experimental true stress-strain curves alongside the J-C model at RT. **Fig 4.15** demonstrates the J-C model at LN and the last, **Fig 4.16**, at 300°C. Despite noticeable variations between experimental results and model prediction, the J-C captures the trends and exhibits differences which are rather expected under such a large temperature range, various deformation mechanisms, and given the rather simple nature of the considered J-C model.

It should be noted that the fits provide the best predictive capability at the reference deformation conditions (-196°C/77K, 1.32e-3/s). However, as the temperature and strain rate increase, the deviation between the experimental and predicted values increase which means that the flow-stress is indirectly related to the strain rate and temperature. The largest variation was observed at the highest deformation temperature of 300 °C. It should be noted here that in the Johnson-Cook model, by assuming that thermal softening, strain rate hardening, and strain hardening are three uncorrelated impacts, the model disregards the coupling impacts of deformation temperature, strain rate, and strain on the flow behavior. In addition, the considered alloy, as shown in this work, exhibits different deformation mechanisms depending on the temperature and strain rate (i.e., slip, TWIP, and TRIP). The strain rate sensitivity for twinning, phase transformation, and crystallographic slip are different. The J-C model does not capture or consider the nature of deformation and is therefore not capable of predicting any variations introduced by switching the deformation mechanisms in response to deformation temperature change.

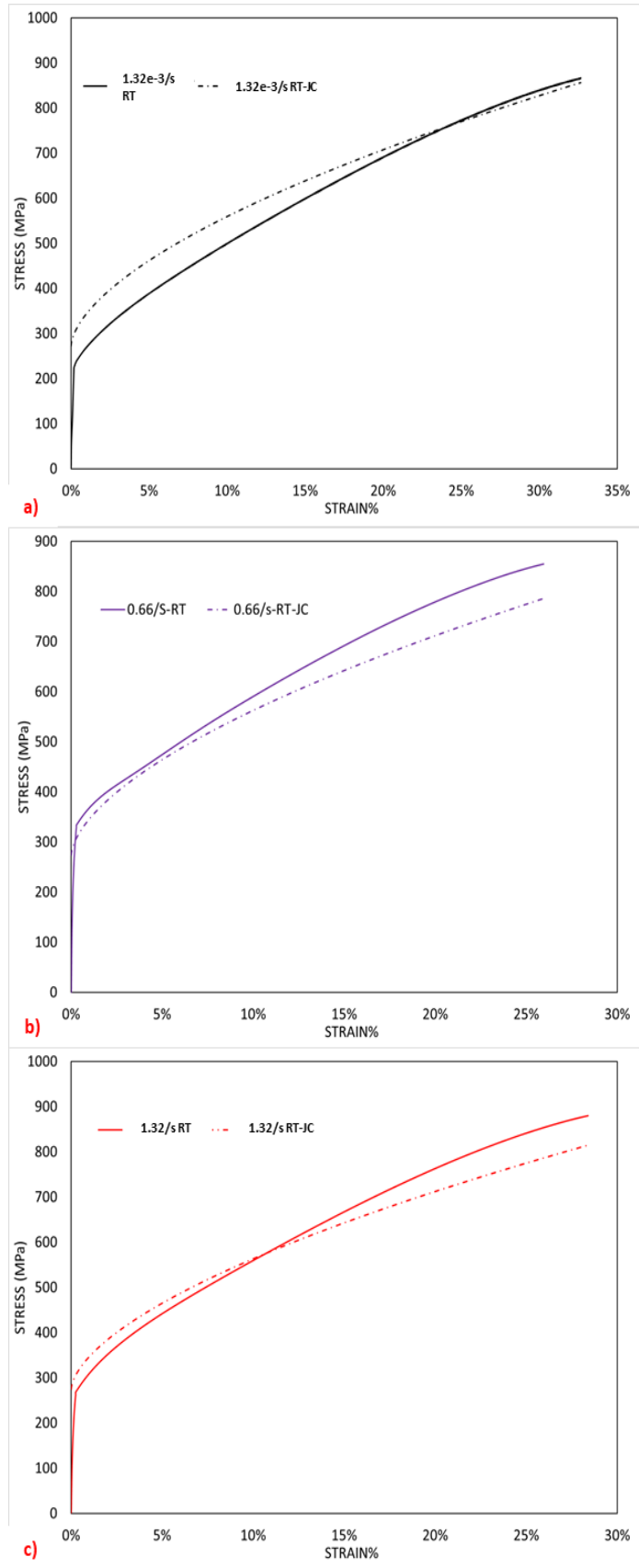


Figure 4.14:JC flow stress model at RT a)  $1.32 \times 10^{-3}$ /s, b) 0.66/s and c) 1.32/s

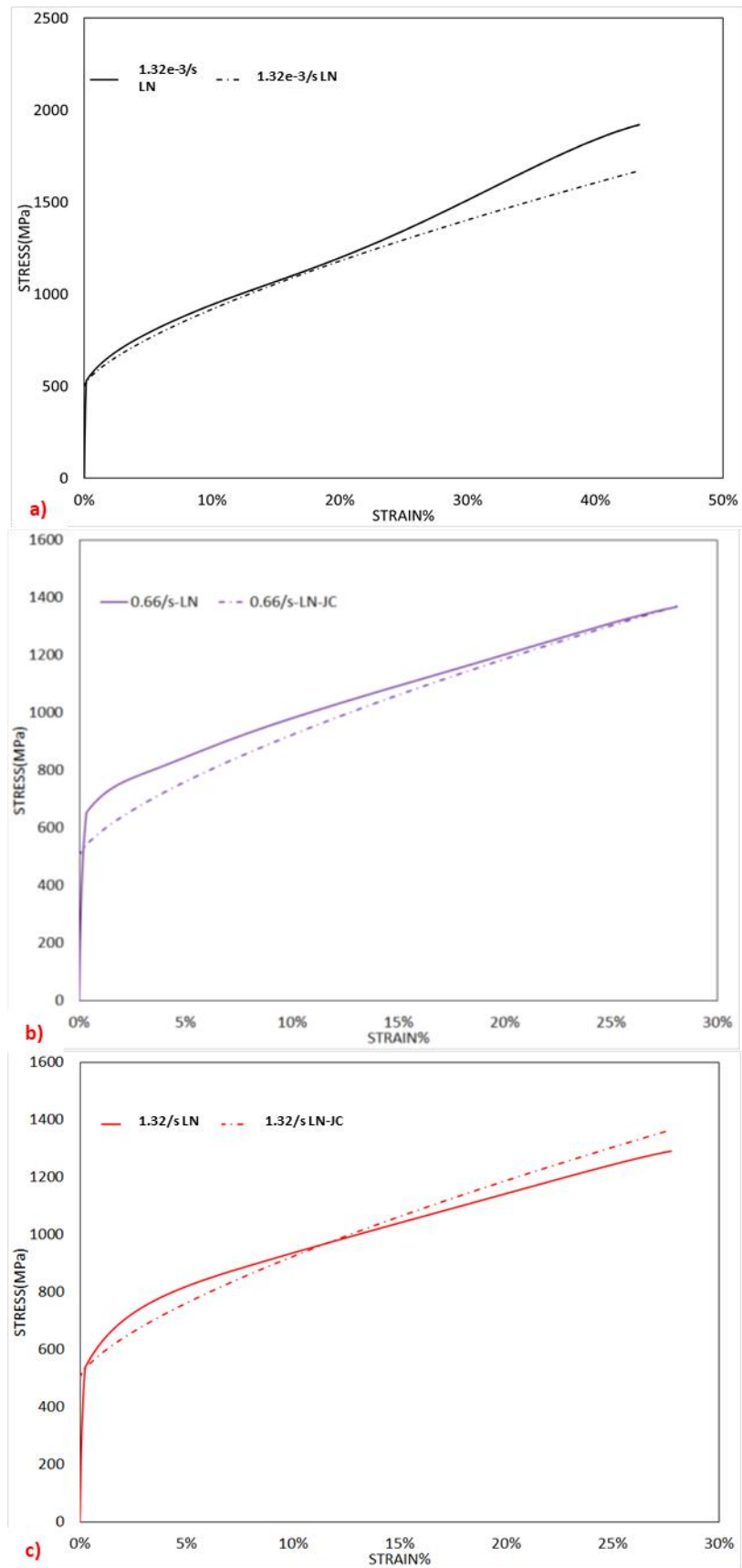


Figure 4.15:JC flow stress model at LN a)  $1.32 \times 10^{-3}$ /s, b) 0.66/s and c) 1.32/s

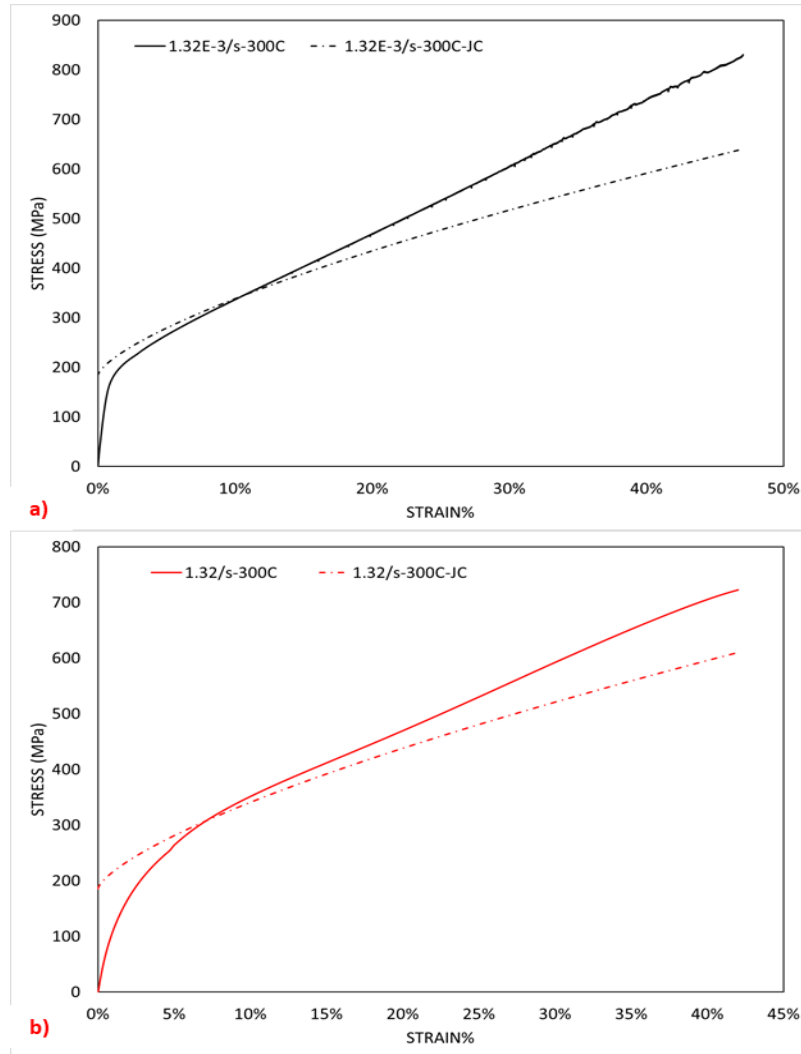


Figure 4.16: flow stress model at 300°C a) 1.32e-/s, b) 1.32/s

**4.6.2 V-A model** This section will discuss the flow stress model developed by Voyiadjis and Abed to simulate the flow stress in pure FCC and BCC metals based on their microstructure at high and low strain rates and temperatures. As it was mentioned before, this model is physics based and derives model parameters based on the microstructure of the alloy. Some of the model parameters were determined for the considered alloy in this study, and will be discussed in the next section however, due to the insufficient data regarding the microstructure, it was crucial to find the parameters from the literature [37][51]. A summary of all the microstructural parameters is shown below in Table 7 and 8.

$$\sigma = Y_a + (\tilde{B}\epsilon_p^n) \left[ 1 - (\beta_1(\epsilon_p)T - \beta_2 T \ln \frac{\dot{\epsilon}_p}{\epsilon_p O^t})^{\frac{1}{q}} \right]^{1/p} \quad (23)$$

**4.6.2.1 Fitting VA model parameters.** Determination of  $b$  (burgers vector) For the cubic FCC structure, the magnitude of the Burgers vector is given in terms of the Miller index  $[h\ k\ l]$  of its direction:  $[110]$

$$\mathbf{b} = (\mathbf{a}_{avg}/2) * (h^2 + k^2 + l^2)^{0.5} \quad (24)$$

where  $\mathbf{a}_{avg}$  is the average lattice parameter obtained by averaging the values of  $\mathbf{a}$  in **Table 1**. To calculate the burgers vector, first the average lattice parameter should be calculated by  $\frac{3.58+3.59+3.56+3.58}{4} = 3.5775$ . The Burgers vector is calculated here based on full dislocation (i.e. slip in the  $[110]$ ) direction. Then using the Equation above (**Eq23**),  $\mathbf{b}$  is found to be 2.5296.

**Determination of  $n$**  To calculate the value of  $n$ , the true stress and true strain are plotted, log-log scale, as shown in Fig 4.14. The slope of the linear established linear fit represents the value of constant  $n = 0.4$ .

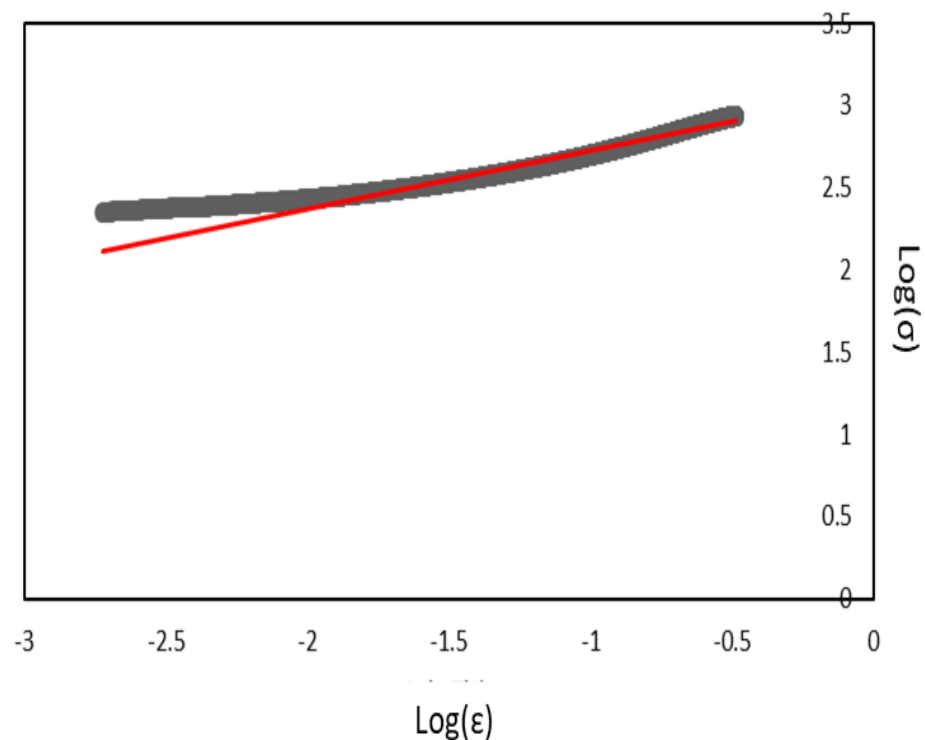


Figure 4.17: log-log curve of the True stress and True strain

**Determination of  $\tilde{B}$**  To calculate  $\tilde{B}$ , Eq 5 was used.  $\tilde{B} = m\alpha_o\mu_o \frac{b^2}{A''_o}$  where  $\alpha_o$  is a constant which represents the portion of the shear modulus  $\mu_o$ ,  $m$  is the orientation factor that relates the shear stress to the normal stress,  $b$  is the magnitude of the Burgers vector and  $A_o$  is the activation area.  $A_o$ ,  $\alpha_o$  were determined through literature along with  $m=\sqrt{3}$ . Parameter that were not found through literature had to be calculated, like  $b$  that has been discussed in section 4.8.1. The other parameter is  $\mu_o$  (shear modulus at 0 K). was calculated using the following Equation.

$$E = 2\mu(1 + \nu) \quad (25)$$

Where  $E$  is the elastic modulus,  $\mu$  is the shear modulus and  $\nu$  is the Poisson's ratio=0.3. By finding the elastic modulus at reference the strain rate  $1.32e-3/s$  for the three different temperatures and solving the Equation above (Eq 25), three points were calculated as shown in Fig 4.18. The value of  $\mu_o$  is the Y intercept, and it's equal to 154.8GPa as shown below.

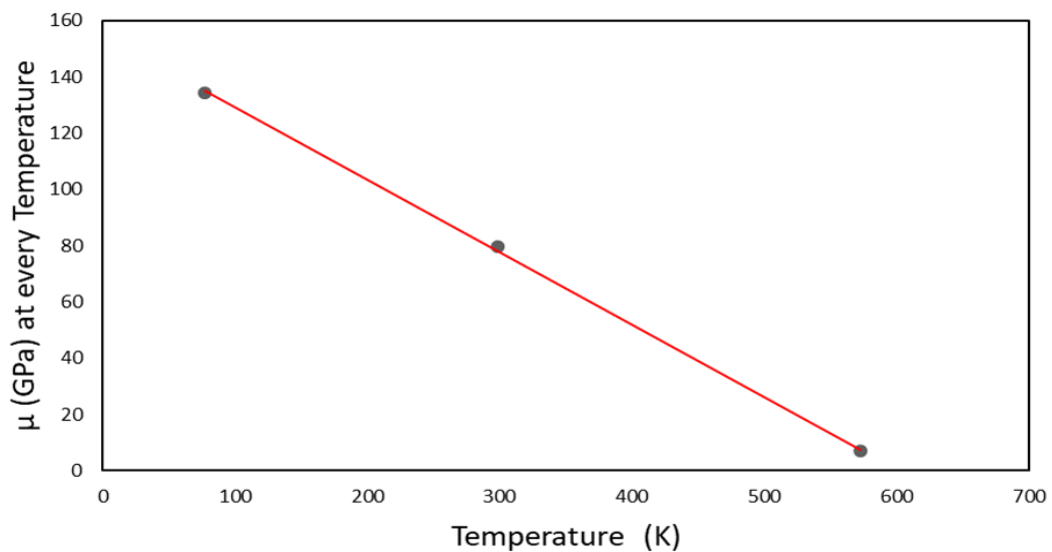


Figure 4.18:  $\mu_o$  linear fit.

Table 7: V-A calculated model parameters

<b>B</b>	<b>1900</b>
<b>n</b>	<b>0.4</b>
<b>b</b>	<b>2.5296</b>
<b><math>\mu_o</math></b>	<b>154800</b>
<b>ya</b>	<b>50</b>

**Remaining model parameters.** All the remaining model parameters were adopted from the literature for similar alloy systems. p and q follow the typical values of 0.5 and 1.5 respectively for all metals. To find C1, the following equation should be used ( $C1 = f \frac{M}{k_a \rho_{mi}}$ ) in the case that the data regarding microstructure is available (the constant in the previous equation are explained in section 2.3.2). However, as some of the required parameters were not available for the considered alloy, C1 was assumed to be 40 which is based on literature, typical for FCC metals.  $\alpha_0$  is typically assumed to be 0.3 for most metals, but in this case,  $\alpha_0 = 0.213$  provided a better fit for the collected data.  $G_0$  which is the Gibbs free energy was assumed to be  $3.8452e-19J$ , typical for FCC metals.  $\beta_1$  was calculated  $\beta_1 = \frac{k}{G_0} \ln(1 + C_1(1 - \exp(-k_a \epsilon_p)))$  where C1 is a constant discussed above,  $k_a$  is the dislocation annihilation factor and  $\epsilon_p$  is the true strain.  $\beta_2$  was found using  $\beta_2 = \frac{k}{G_0}$  where  $\kappa$  is the Avogadro's number and  $G_0$  is the Gibbs free energy. Finally,  $A''_0$  was found using  $A''_0 = 30b^2$  where b is the burgers vector. All assumptions that were made regarding the parameters was in correlation with [37].

Table 8: remaining parameters obtained from literature[37] for FCC alloy

<b>q</b>	<b>1.5</b>	<b>G<sub>0</sub></b>	<b>3.85E-19</b>
<b>p</b>	<b>0.5</b>	<b>β<sub>2</sub></b>	<b>3.59E-05</b>
<b>C1</b>	<b>40</b>	<b>A''<sub>0</sub></b>	<b>191.9663</b>
<b>α<sub>0</sub></b>	<b>0.213</b>	<b>κ</b>	<b>1.38E-23</b>

**Figs 4.19** through **4.21** show the experimental true stress-strain graph alongside the VA flow stress model results. The additional fitting and microstructural parameters contribute to the better fits obtained using the VA model. **Fig 4.19 a through c** show the true stress-strain curves with the VA model for all the considered cases at RT. By comparing these curves with the curves obtained by using the JC model, it is clear that the VA model is much more accurate than JC model. **Fig 4.20 a through c** show the true stress-strain curves with the VA model for all the considered cases at LN. **Fig 4.20b and c** clearly show that the experimental data and the VA model are in line. **Figs 4.20a**, is not particularly aligned with the experimental stress-strain curves, and this may be

due to the fact that the parameters that are used in this model are found through literature and not by EBSD and other ex-situ tools. **4.21a**, and **4.21b** are the two curves that are not in accordance to how the VA model should behave and this is also due to the fact that the parameters that are used in this model are found through literature.

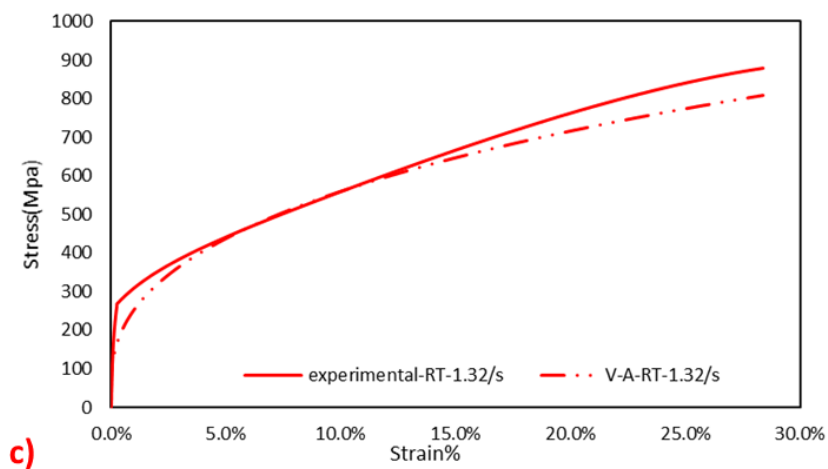
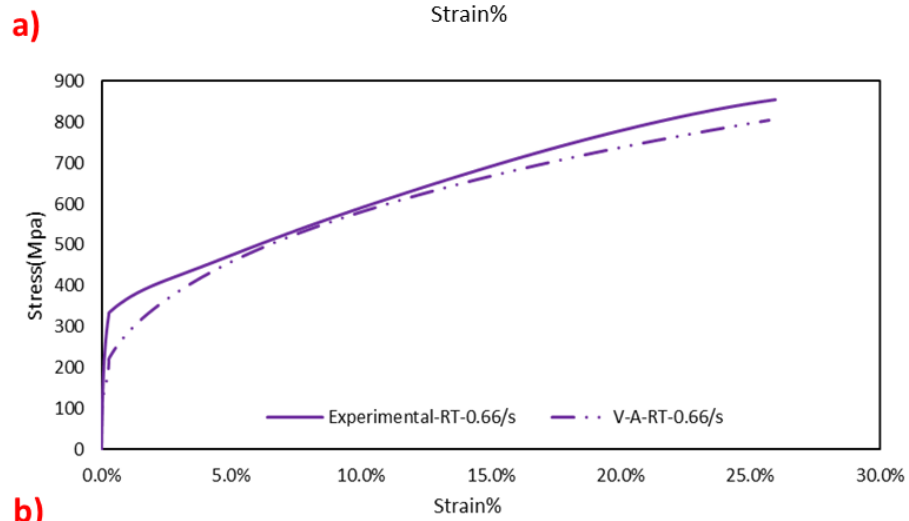
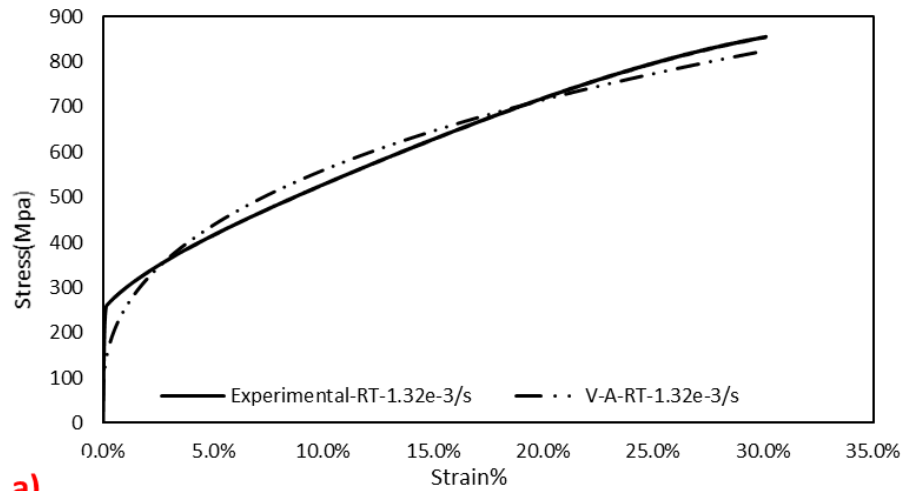


Figure 4.19: VA flow stress model at RT a)  $1.32e-3/s$ , b)  $0.66/s$  and c)  $1.32/s$

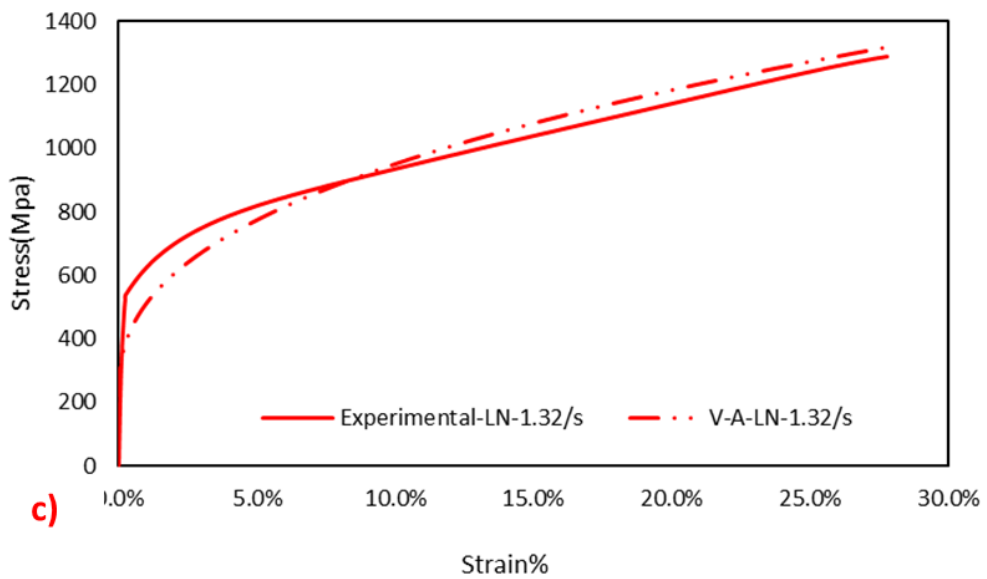
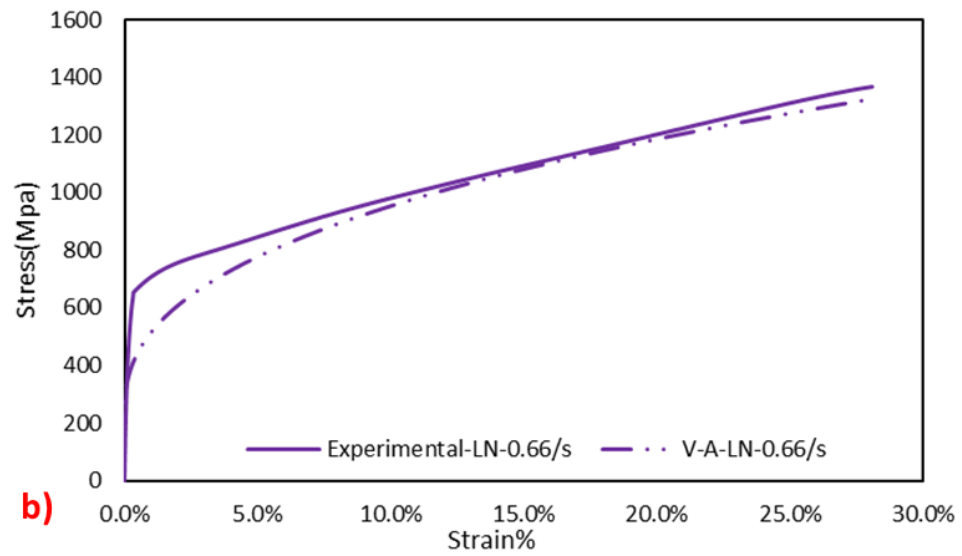
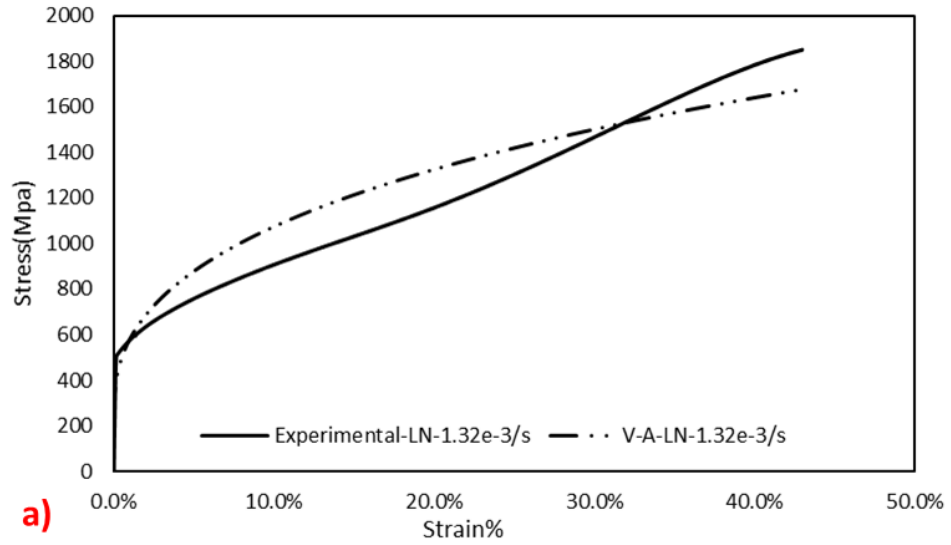


Figure 4.20:VA flow stress model at LN a)1.32e-/s, b) 0.66/s and c) 1.32/s

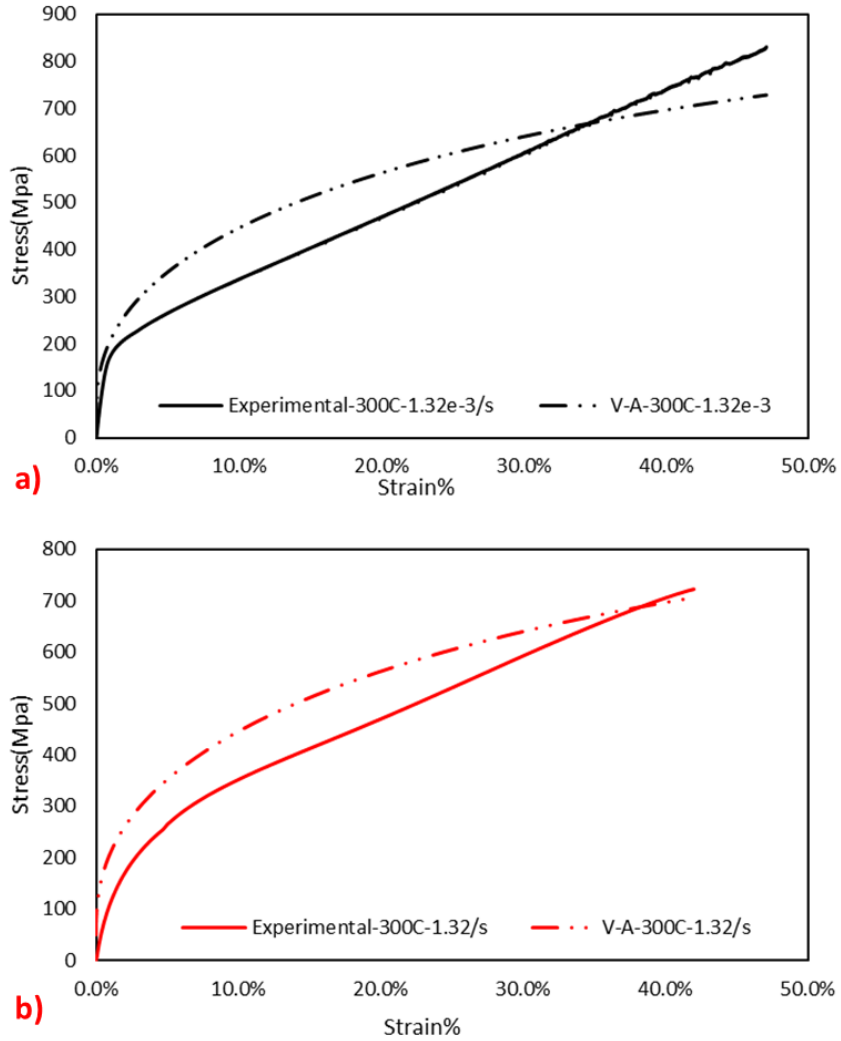


Figure 4.21:VA flow stress model at 300°C a)1.32e-/s, b) 1.32/s

It should be pointed out the both the VA and JC models capture the stress and strain values of the experimental data to a large extent, however variations were also observed. Despite the large number of fitting and microstructurally informed parameters, in particular for the VA model, both equations don't consider deformation twinning and phase transformation. Therefore, as the deformation temperature and rate are altered, the changes in response (e.g., extra hardening) induced by TWIP or TRIP not are captured using these models. Models capable of capturing the effect of TWIP or TRIP (not at the same time) have been proposed in the literature. As additional microstructural data (e.g., EBSD) and accurate measurements of the critical stresses for twinning and transformation are required, the calibration of such constitutive models is left for future work.

## Chapter5. Conclusion

In this work, the non-equiatomic V10F45Co30Cr10Ni5 HEA was investigated at room temperature (298K/25°C), cryogenic temperature (77K/-196°C), and elevated temperature (573K/300°C) at a range of strain rate, 1.32e-3/s, 0.66/s and 1.32/s. The study aimed to enhance the understanding of the effects of TRIP/TWIP of the deformation response of this novel alloy system. The main findings of this study are as follows:

- Increasing the deformation temperature to 300°C resulted in enhanced ductility levels; however, a significant reduction in strength was noted.
- The highest Ultimate Tensile strength (UTS) of 1225 MPa was achieved at cryogenic temperatures and ductility of 62.2 %.
- SRS parameter **m** decreases as the temperature decreased from room temperature to cryogenic temperatures (LN), which indicates a lower strain sensitivity at the cryogenic temperature.
- SRS parameter **m** for samples tested at 77K are lower than those tested at Room Temperature (RT); the lower value of **m** is attributed to twinning, hence the material exhibited TWIP.
- TRIP was present in the samples tested under Cryogenic temperature (FCC to BCC), which gave the material high strength and ductility.
- TWIP was observed through the second stage of strain hardening at RT at 0.66/s.

## Reference

- [1] Zhang, Y., 2021. *history of high entropy materials*. [online] Available at: <[https://www.researchgate.net/publication/333415875\\_History\\_of\\_High-Entropy\\_Materials](https://www.researchgate.net/publication/333415875_History_of_High-Entropy_Materials)> [Accessed 19 July 2021].
- [2] T.Yamada, E.Abe, C.Osawa, and N.Yukawa, Prediction on microstructure and mechanical properties of hot forged Ni-based super alloy by optimization using genetic algorithms. *Procedia Manufacturing*, vol.15, pp.356-363, 2018.
- [3] S. Dehgahi, R. Alaghmandfard, J. Tallon, A. Odeshi, and M. Mohammadi, “A Microstructural evolution and high strain rate compressive behavior of as-built and heat-treated additively manufactured maraging steels,” *Mater. Sci. Eng. A*, vol. 815, no. December 2020, p. 141183, 2021, doi: 10.1016/j.msea.2021.141183.
- [4] W. Abuzaid, M. Egilmez, and Y. I. Chumlyakov, “TWIP – TRIP effect in single crystalline VFeCoCrNi multi-principle element alloy,” *Scr. Mater.*, vol. 194, p. 113637, 2021, doi: 10.1016/j.scriptamat.2020.113637.
- [5] R.Mishra, R.Haridas and P.Agrawal. High entropy alloys – Tunability of deformation mechanisms through integration of compositional and microstructural domains. *Materials Science and Engineering: A*, vol. 812, p.141085, 2021.
- [6] T. Chen, M. Wong, T. Shun, and J. Yeh, “Nanostructured nitride films of multi-element high-entropy alloys by reactive DC sputtering,” vol. 200, pp. 1361–1365, 2005, doi: 10.1016/j.surfcoat.2005.08.081.
- [7] I. V. Kireeva, Y. I. Chumlyakov, Z. V. Pobedennaya, A. V. Vyrodova, and I. Karaman, “Twinning in [001]-oriented single crystals of CoCrFeMnNi high-entropy alloy at tensile deformation,” *Mater. Sci. Eng. A*, vol. 713, no. December 2017, pp. 253–259, 2018, doi: 10.1016/j.msea.2017.12.059.
- [8] Z. F. He, N. Jia, D. Ma, H. L. Yan, Z. M. Li, and D. Raabe, “Joint contribution of transformation and twinning to the high strength-ductility combination of a FeMnCoCr high entropy alloy at cryogenic temperatures,” *Mater. Sci. Eng. A*, vol. 759, no. April, pp. 437–447, 2019, doi: 10.1016/j.msea.2019.05.057.
- [9] E. P. George, D. Raabe, and R. O. Ritchie, “High-entropy alloys,” *Nat. Rev. Mater.*, vol. 4, no. 8, pp. 515–534, 2019, doi: 10.1038/s41578-019-0121-4.
- [10] G. Laplanche, A. Kostka, O. M. Horst, G. Eggeler, and E. P. George, “Microstructure evolution and critical stress for twinning in the CrMnFeCoNi high-entropy alloy,” *Acta Mater.*, vol. 118, pp. 152–163, 2016, doi: 10.1016/j.actamat.2016.07.038.
- [11] Z.He, N.Jia, H.Wang, Y.Liu, D.Li and Y.Shen. The effect of strain rate on mechanical properties and microstructure of a metastable FeMnCoCr high entropy alloy. *Materials Science and Engineering: A*, vol. 776, p.138982, 2020.
- [12] W. Abuzaid and H. Sehitoglu, “Critical resolved shear stress for slip and twin nucleation in single crystalline FeNiCoCrMn high entropy alloy,” *Mater.*

- Charact.*, vol. 129, no. May, pp. 288–299, 2017, doi: 10.1016/j.matchar.2017.05.014.
- [13] Z.He, N.Jia, H.Wang, Y.Liu, D.Li and Y.Shen. The effect of strain rate on mechanical properties and microstructure of a metastable FeMnCoCr high entropy alloy. *Materials Science and Engineering: A*, vol. 776, p.138982, 2020.
- [14] Z. Li, F. Körmann, B. Grabowski, J. Neugebauer, and D. Raabe, “Ab initio assisted design of quinary dual-phase high-entropy alloys with transformation-induced plasticity,” *Acta Mater.*, vol. 136, pp. 262–270, 2017, doi: 10.1016/j.actamat.2017.07.023.
- [15] Jo, Y., Yang, J., Doh, K., An, W., Kim, D., Sung, H., Lee, D., Kim, H., Sohn, S. and Lee, S. Analysis of damage-tolerance of TRIP-assisted V10Cr10Fe45Co30Ni5 high-entropy alloy at room and cryogenic temperatures. *Journal of Alloys and Compounds*, vol. 844, p.156090, 2020.
- [16] Jo, Y., Kim, D., Jo, M., Doh, K., Sohn, S., Lee, D., Kim, H., Lee, B. and Lee, S.. Effects of deformation–induced BCC martensitic transformation and twinning on impact toughness and dynamic tensile response in metastable VCrFeCoNi high–entropy alloy. *Journal of Alloys and Compounds*, vol. 785, pp.1056-1067, 2019.
- [17] J.Yang, Y. Jo, D.Kim, W.Choi, H.Kim, B.Lee, S.Sohn and S.Lee. “A Effects of transformation-induced plasticity ( TRIP ) on tensile property improvement of Fe 45 Co 30 Cr 10 V 10 Ni 5-x Mn x high-entropy alloys,” vol. 772, no. December 2019, 2020.
- [18] W. Huo, H. Zhou, F. Fang, X. Hu, Z. Xie, and J. Jiang, “Strain-rate effect upon the tensile behavior of CoCrFeNi high-entropy alloys,” *Mater. Sci. Eng. A*, vol. 689, no. December 2016, pp. 366–369, 2017, doi: 10.1016/j.msea.2017.02.077.
- [19] S. Basu, Z. Li, K. G. Pradeep, and D. Raabe, “Strain rate sensitivity of a TRIP-assisted dual-phase high-entropy alloy,” *Front. Mater.*, vol. 5, no. May, pp. 1–10, 2018, doi: 10.3389/fmats.2018.00030.
- [20] Z. Wang, W. Lu, D. Raabe, and Z. Li, “On the mechanism of extraordinary strain hardening in an interstitial high-entropy alloy under cryogenic conditions,” *J. Alloys Compd.*, vol. 781, pp. 734–743, 2019, doi: 10.1016/j.jallcom.2018.12.061.
- [21] A. Gali and E. P. George, “Tensile properties of high- and medium-entropy alloys,” *Intermetallics*, vol. 39, pp. 74–78, 2013, doi: 10.1016/j.intermet.2013.03.018.
- [22] T.Zhang, R. Zhao, F.Wu, S.Lin, S.Jiang, Y.Huang, S.Chen and J.Eckert. “Transformation-enhanced strength and ductility in a FeCoCrNiMn dual phase high-entropy alloy,” *Mater. Sci. Eng. A*, vol. 780, no. February, 2020, doi: 10.1016/j.msea.2020.139182.
- [23] S. Gangireddy, L. Kaimiao, B. Gwalani, and R. Mishra, “Microstructural dependence of strain rate sensitivity in thermomechanically processed Al0.1CoCrFeNi high entropy alloy,” *Mater. Sci. Eng. A*, vol. 727, no. March, pp. 148–159, 2018, doi: 10.1016/j.msea.2018.04.108.

- [24] S. Zhang, Z. Wang, H. J. Yang, J. W. Qiao, Z. H. Wang, and Y. C. Wu, “Ultra-high strain-rate strengthening in ductile refractory high entropy alloys upon dynamic loading,” *Intermetallics*, vol. 121, no. April, pp. 1–7, 2020, doi: 10.1016/j.intermet.2020.106699.
- [25] R. Sonkusare, R. Jain, K. Biswas, V. Parameswaran, and N. P. Gurao, “High strain rate compression behaviour of single phase CoCuFeMnNi high entropy alloy,” *J. Alloys Compd.*, vol. 823, p. 153763, 2020, doi: 10.1016/j.jallcom.2020.153763.
- [26] M. lei Hu, W. dong Song, D. bo Duan, and Y. Wu, “Dynamic behavior and microstructure characterization of TaNbHfZrTi high-entropy alloy at a wide range of strain rates and temperatures,” *Int. J. Mech. Sci.*, vol. 182, no. April, p. 105738, 2020, doi: 10.1016/j.ijmecsci.2020.105738.
- [27] Y. Xiao, R. Kozak, M. Haché, W. Steurer, R. Spolenak, J. Wheeler and Y. Zou “Micro-compression studies of face-centered cubic and body-centered cubic high-entropy alloys: Size-dependent strength, strain rate sensitivity, and activation volumes,” *Mater. Sci. Eng. A*, vol. 790, no. February, 2020, doi: 10.1016/j.msea.2020.139429.
- [28] I. V. Kireeva, Y. I. Chumlyakov, A. V. Vyrodova, Z. V. Pobedennaya, and I. Karaman, “Effect of twinning on the orientation dependence of mechanical behaviour and fracture in single crystals of the equiatomic CoCrFeMnNi high-entropy alloy at 77K,” *Mater. Sci. Eng. A*, vol. 784, no. March, p. 139315, 2020, doi: 10.1016/j.msea.2020.139315.
- [29] W. Fu *et al.*, “Cryogenic mechanical behaviors of CrMnFeCoNi high-entropy alloy,” *Mater. Sci. Eng. A*, vol. 789, no. December 2019, p. 139579, 2020, doi: 10.1016/j.msea.2020.139579.
- [30] S. Picak, J. Liu, C. Hayrettin, W. Nasim, D. Canadinc, K. Xie, Y. Chumlyakov, I. Kireeva AND I. Karaman. “Anomalous work hardening behavior of Fe<sub>40</sub>Mn<sub>40</sub>Cr<sub>10</sub>Co<sub>10</sub> high entropy alloy single crystals deformed by twinning and slip,” *Acta Mater.*, vol. 181, pp. 555–569, 2019, doi: 10.1016/j.actamat.2019.09.048.
- [31] H. Y. Yasuda, K. Shigeno, and T. Nagase, “Dynamic strain aging of Al<sub>0.3</sub>CoCrFeNi high entropy alloy single crystals,” *Scr. Mater.*, vol. 108, pp. 80–83, 2015, doi: 10.1016/j.scriptamat.2015.06.022.
- [32] I. V. Kireeva, Y. I. Chumlyakov, Z. V. Pobedennaya, and A. V. Vyrodova, “Effect of  $\gamma'$ -phase particles on the orientation and temperature dependence of the mechanical behaviour of Al<sub>0.3</sub>CoCrFeNi high-entropy alloy single crystals,” *Mater. Sci. Eng. A*, vol. 772, no. September 2019, p. 138772, 2020, doi: 10.1016/j.msea.2019.138772.
- [33] I. V. Kireeva, Y. I. Chumlyakov, Z. V. Pobedennaya, A. V. Vyrodova, I. V. Kuksgauzen, and D. A. Kuksgauzen, “Orientation and temperature dependence of a planar slip and twinning in single crystals of Al<sub>0.3</sub>CoCrFeNi high-entropy alloy,” *Mater. Sci. Eng. A*, vol. 737, no. September, pp. 47–60, 2018, doi: 10.1016/j.msea.2018.09.025.

- [34] S.Ma, S.Zhang, J.Qiao, Z.Wang, M.Gao, Z.Jiao, H.Yang, Y.Zhang, “Superior high tensile elongation of a single-crystal CoCrFeNiAl 0.3 high-entropy alloy by Bridgman solidification,” *Intermetallics*, vol. 54, pp. 104–109, 2014, doi: 10.1016/j.intermet.2014.05.018.
- [35] I. V. Kireeva, Y. I. Chumlyakov, A. V. Vyrodova, Z. V. Pobedennaya, and I. Karaman, “Effect of twinning on the orientation dependence of mechanical behaviour and fracture in single crystals of the equiatomic CoCrFeMnNi high-entropy alloy at 77K,” *Mater. Sci. Eng. A*, vol. 784, no. January, p. 139315, 2020, doi: 10.1016/j.msea.2020.139315.
- [36] J. Li, F. Li, J. Cai, R. Wang, Z. Yuan, and G. Ji, “Comparative investigation on the modified Zerilli-Armstrong model and Arrhenius-type model to predict the elevated-temperature flow behaviour of 7050 aluminium alloy,” *Comput. Mater. Sci.*, vol. 71, pp. 56–65, 2013, doi: 10.1016/j.commatsci.2013.01.010.
- [37] G. Z. Voyiadjis and F. H. Abed, “Effect of dislocation density evolution on the thermomechanical response of metals with different crystal structures at low and high strain rates and temperatures,” *Arch. Mech.*, vol. 57, no. 4, pp. 299–343, 2005, doi: 10.24423/aom.190.
- [38] D. T. Pierce, J. A. Jiménez, J. Bentley, D. Raabe, and J. E. Wittig, “The influence of stacking fault energy on the microstructural and strain-hardening evolution of Fe-Mn-Al-Si steels during tensile deformation,” *Acta Mater.*, vol. 100, pp. 178–190, 2015, doi: 10.1016/j.actamat.2015.08.030.
- [39] X. Gao, Y. Lu, J. Liu, J. Wang, T. Wang, and Y. Zhao, “Extraordinary ductility and strain hardening of Cr<sub>26</sub>Mn<sub>20</sub>Fe<sub>20</sub>Co<sub>20</sub>Ni<sub>14</sub> TWIP high-entropy alloy by cooperative planar slipping and twinning,” *Materialia*, vol. 8, no. September, p. 100485, 2019, doi: 10.1016/j.mtla.2019.100485.
- [40] Peijun Yu, Rui Feng, Junping Du, Shuhei Shinzato, Jyh-Pin Chou, Bilin Chen, Yu-Chieh Lo, Peter K. Liaw, Shigenobu Ogata, Alice Hu, “Phase transformation assisted twinning in a face-centered-cubic FeCrNiCoAl<sub>0.36</sub> high entropy alloy,” *Acta Mater.*, vol. 181, pp. 491–500, 2019, doi: 10.1016/j.actamat.2019.10.012.
- [41] H. U. Jeong and N. Park, “TWIP and TRIP-associated mechanical behaviors of Fe<sub>x</sub>(CoCrMnNi)<sub>100-x</sub> medium-entropy ferrous alloys,” *Mater. Sci. Eng. A*, vol. 782, no. December 2019, p. 138896, 2020, doi: 10.1016/j.msea.2019.138896.
- [42] X. Ji, S. Emura, X. Min, and K. Tsuchiya, “Strain-rate Effect on Work-hardening Behavior in  $\beta$  -type Ti-10Mo-1Fe Alloy with TWIP Effect Materials Science & Engineering A Strain-rate effect on work-hardening behavior in  $\beta$  -type Ti-10Mo-1Fe alloy with TWIP effect,” *Mater. Sci. Eng. A*, vol. 707, no. November, pp. 701–707, 2017, doi: 10.1016/j.msea.2017.09.055.
- [43] Z.Han, W.Ren, J.Yang, Y.Du, R.Wei, C.Zhang, Y.Chen, G.Zhang., “The deformation behavior and strain rate sensitivity of ultra-fine grained CoNiFeCrMn high-entropy alloys at temperatures ranging from 77 K to 573 K,” *J. Alloys Compd.*, vol. 791, pp. 962–970, 2019, doi: 10.1016/j.jallcom.2019.03.373.
- [44] H. Becker and W. Pantleon, “Work-hardening stages and deformation

- mechanism maps during tensile deformation of commercially pure titanium,” *Comput. Mater. Sci.*, vol. 76, pp. 52–59, 2013, doi: 10.1016/j.commatsci.2013.03.028.
- [45] S. K. Sahoo, S. Biswas, L. S. Toth, P. C. Gautam, and B. Beausir, “Strain hardening, twinning and texture evolution in magnesium alloy using the all twin variant polycrystal modelling approach,” *Int. J. Plast.*, vol. 128, no. January, p. 102660, 2020, doi: 10.1016/j.ijplas.2020.102660.
- [46] F. Hamdi and S. Asgari, “Influence of stacking fault energy and short-range ordering on dynamic recovery and work hardening behavior of copper alloys,” *Scr. Mater.*, vol. 62, no. 9, pp. 693–696, 2010, doi: 10.1016/j.scriptamat.2010.01.031.
- [47] Rollett, A. and Kocks, U. A Review of the Stages of Work Hardening. *Solid State Phenomena*, 35-36, pp.1-18,1993.
- [48] Dong, Y., Sun, Z., Xia, H., Feng, J., Du, J., Fang, W., Liu, B., Wang, G., Li, L., Zhang, X. and Yin, F., 2018. The Influence of Warm Rolling Reduction on Microstructure Evolution, Tensile Deformation Mechanism and Mechanical Properties of an Fe-30Mn-4Si-2Al TRIP/TWIP Steel”, *Metals*, vol. 8, no. 10, p. 742, 2018. Available: 10.3390/met8100742.
- [49] G. Zhao, X. Xu, D. Dye, and P. E. J. Rivera-díaz-del-castillo, “Acta Materialia Microstructural evolution and strain-hardening in TWIP Ti alloys,” *Acta Mater.*, vol. 183, pp. 155–164, 2020, doi: 10.1016/j.actamat.2019.11.009.
- [50] S. L. Wong, M. Madivala, U. Prahl, F. Roters, and D. Raabe, “A crystal plasticity model for twinning- and transformation-induced plasticity,” *Acta Mater.*, vol. 118, pp. 140–151, 2016, doi: 10.1016/j.actamat.2016.07.032.
- [51] Yong Hee Jo, Junha Yang, Kyung-Yeon Doh, Woojin An, Dae Woong Kim, Hyokyung Sung, Donghwa Lee, Hyoung Seop Kim, Seok Su Sohn, Sunghak Lee, “Analysis of damage-tolerance of TRIP-assisted V 10 Cr 10 Fe 45 Co 30 Ni 5 high-entropy alloy at room and cryogenic temperatures,” *J. Alloys Compd.*, vol. 844, p. 156090, 2020, doi: 10.1016/j.jallcom.2020.156090.

### **Vita**

Omar Mohammad Marwan El Batal was born in 1997, in Beirut, Lebanon and moved to the UAE in 1998. He was educated in the local schools of UAE and graduated from Dubai international school in 2014.

In 2014 Mr. Omar enrolled in the Emirates Aviation University to earn a degree in Aeronautical engineering in 2018, after which he enrolled in AUS to continue his studies in mechanical engineering. During his studies Omar worked with Dr.Wael Abuzaid as a graduate research assistant, they worked mostly on high entropy alloys and shape memory alloys.